

The Cloud Resolving Model Radar Simulator (CR-SIM) Version 3.3: Description and Applications of a Virtual Observatory

Mariko Oue¹, Aleksandra Tatarevic², Pavlos Kollias^{1,3}, Dié Wang³, Kwangmin Yu⁴, Andrew M. Vogelmann³

- 5 1. School of Marine and Atmospheric Sciences, Stony Brook University, Stony Brook, 11794, USA
2. Department of Atmospheric and Oceanic Sciences, McGill University, Montreal, H3A 0G4, Canada
3. Environmental and Climate Sciences Department, Brookhaven National Laboratory, Upton, 11973, USA
4. Computational Science Initiative, Brookhaven National Laboratory, Upton, 11973, USA

Correspondence to: Mariko Oue (mariko.oue@stonybrook.edu)

10 **Abstract.** Ground-based observatories use multi-sensor observations to characterize cloud and precipitation properties. A challenge is how to design strategies to best use these observations to understand the atmosphere and evaluate atmospheric numerical prediction models. This paper introduces the Cloud resolving model Radar SIMulator (CR-SIM), which uses output from high-resolution atmospheric models to emulate multi-wavelength, zenith-pointing, and scanning radar observables and multi-sensor (multi-radar and radar-lidar) integrated products. CR-SIM allows comparisons of the same variables between an
15 atmospheric model simulation and remote sensing products using a forward modeling framework consistent with the microphysical assumptions used in the numerical model simulations. In this paper, we present several applications of CR-SIM for evaluation of a numerical model, quantification of retrieval uncertainty, and optimization of radar sampling strategy using observing system simulation experiments. These applications demonstrate that the application of CR-SIM as a virtual observatory operator on high-resolution model output helps interpret the differences between model results and observations
20 and also improve understanding of the representativeness errors due to the sampling limitations of the ground-based observatories. CR-SIM is licensed under the GNU GPL package and both the software and the user guide are freely available to scientific community.

1 Introduction

Ground-based observatories offer an integrated view of cloud and precipitation systems complementary to that available
25 from satellites with excellent vertical resolution, especially in the boundary layer, and an accompanying description of the large-scale forcing. Today, a number of observatories are continuously operated in different climate regimes (Illingworth et al., 2007; Löhnert et al., 2015; Stevens et al., 2016; Mather et al., 2016) with evolving measurement capabilities. In the beginning, zenith-pointing cloud radars, lidars, and radiometers provided the primary cloud and precipitation measurements. Recently, the need to characterize the mesoscale organization of clouds and precipitation over a larger domain has heightened
30 the sophistication and complexity of these observatories to go beyond single, one-dimensional profiling measurements. For

example, the U.S. Department of Energy (DOE) Atmospheric Radiation Measurement (ARM) observatories offer observations from distributed networks of profiling and scanning radars, lidars, and radiometers (Turner and Ellingson, 2016; North et al., 2017).

35 Multi-parametric information from profiling and scanning radars, lidars, and radiometers has been used to retrieve cloud
microphysical and kinematic properties, such as hydrometeor mixing ratio and number concentration (e.g., Zhang et al., 2014)
and ice particle properties (e.g., Kneifel et al. 2015; 2016; Matrosov et al. 2017; Von Lerber et al., 2017). However, the
comparison between the retrieved observables (e.g., ice water content from radar reflectivity) and model-produced parameters
often involves large uncertainties. Several factors, not limited to the nature of ground-based observations, challenge model
evaluation using observations. In many cases, the retrieval algorithms are based on statistical estimation of ill-posed inverse
40 problems, and the results may not capture well the observed variability of natural data because of limitations from assumptions
embedded in the retrieval algorithms (e.g., Szyrmer et al., 2012; Szyrmer and Zawadzki, 2014). Furthermore, determining
critical parameters for model evaluation such as the cloud fraction profile requires complimentary, synergistic observations
from radar and lidar. One such example is the Active Remotely-Sensed Cloud Location (ARSCL, Clothiaux et al., 2001)
product that combines radar and lidar data to estimate hydrometeor location in the column. Other examples of critical
45 parameters that require a multi-sensor approach include cloud and precipitation classification schemes (Illingworth et al., 2007)
and hydrometeor phase classification (e.g., Shupe, 2007; Luke et al., 2010; Lamer et al., 2018). So, how do we best compare
such products developed using multiple sensors with different capabilities (i.e., sensitivity) with numerical model output?
Additionally, challenges may arise from the sampling strategy used to obtain the observations. For example, a recent study has
shown that profiling observations from one location are inadequate in representing statistically robust domain cloud properties
50 such as cloud fraction profile (Oue et al., 2016). A similar investigation on 3D wind retrievals in deep convection using multi-
Doppler radar techniques highlighted similar deficiencies of our current observing systems (Oue et al., 2019a). How do we
best quantify the measurement uncertainty introduced by the observational strategy?

In this paper, we introduce the Cloud Resolving Model (CRM) Radar Simulator (CR-SIM), which has been continuously
developed over the last five years to facilitate improvement of model-observation comparisons. CR-SIM applies forward
55 simulators to atmospheric model output to simulate sensor measurements. These sensor simulations may be used: (1) to
compare directly to the measurements, for an apples-to-apples comparison in sensor variables, or (2) as input to retrieval
algorithms to assess the retrieval methodology or sampling strategy using the original atmospheric model output as ‘truth.’
Here, the CR-SIM architecture and capabilities are presented along with a series of forward simulations that emphasize its
capabilities. In particular, we highlight the applications of CR-SIM in investigations of observational uncertainties. Although
60 accurate estimation of uncertainties in the observation retrieval products (e.g., ice water content, liquid water content, vertical
velocity) is challenging, forward simulators allow us to emulate the observational retrieval products accounting for known
error sources to understand the exact impacts of those error sources on the products by comparisons with the ‘truth,’ which is
usually the input model data. Observing system simulation experiments (OSSEs) take advantage of forward modelling to
produce simulated measurements. The understanding from OSSEs would help: i) evaluate the model simulations using the

65 observations accounting for the observation limitations, ii) estimate uncertainties in applied retrieval techniques, iii) propose
a new retrieval technique accounting for its uncertainty, and iv) optimize new observation system strategy. This study
demonstrates the application of the CR-SIM forward simulator in several OSSEs in which ARM multi-sensor products, such
as cloud locations and vertical velocity, are evaluated by considering limitations inherently imposed by the nature of
observations. (A list of acronyms is provided after the Summary for easy reference.)

70

2. Forward Simulators

Forward simulators have been widely used to design observing systems and to provide an alternative path to model-
observation comparisons by transforming the model geophysical quantities into remote sensing observables. There are several
75 sophisticated radar simulators, which have been developed for specialized applications of interest. For example, Snyder et al.
(2017a, 2017b) simulated polarimetric radar characteristics of a supercell using radar forward simulators to understand the
contribution of microphysical characteristics to the polarimetric characteristics and their wavelength dependency. They
accounted for the water fraction of solid ice particles to realistically simulate differential reflectivity (Z_{DR}) columns, specific
differential phase (K_{DP}) columns, and co-polar correlation coefficient (ρ_{HV}) rings in supercells. A cloud radar simulator
80 developed by Zhang et al. (2018) is designed to simulate vertically pointing cloud radar reflectivity (e.g., Ka- and W-band
radars) from global climate model (GCM) data. This is beneficial for comparison of datasets of different scales (cloud-scale
observational data versus global-scale data). Matsui et al. (2019) simulated polarimetric precipitation radar-based hydrometeor
classification, vertical velocity, and rain rate from CRM output to examine uncertainties in the retrieval algorithms and model
microphysical parameterizations using POLARRIS. The uncertainties are attributed to assumptions of hydrometeor particle
85 size distribution, density, axis ratio, and canting angle. Lamer et al. (2018) developed the GCM-oriented ground-observation
forward-simulator ((GO)²-SIM), a comprehensive radar-lidar simulator for GCMs, that emulates radar Doppler spectra
moments, lidar backscatter and depolarization, and provides synthetic estimates of mixed-phased cloud occurrence in the GCM
that are compared to those estimated from observations using the same methodology.

CR-SIM has the capability of simulating the ideal and propagation-corrected multi-wavelength radar and lidar
90 observables, and multi-sensor integrated products. The zenith-pointing and scanning radar observables include radar
reflectivity, Doppler velocity, spectrum width, and polarimetric fields. Zenith-pointing lidar observables include lidar
backscatter and extinction coefficient. The idea behind CR-SIM is to have a forward model operator that provides *idealized*
radar and lidar observables (i.e., actual observations after perfect quality control and correction for the propagation effects) on
the same grid as in the CRMs or large-eddy simulations (LESs) to facilitate model-observation comparisons. Further, the
95 design is flexible enough to be coupled with different microphysical schemes and different scattering methods (e.g., T-matrix,
Mishchenko, 2000; Discrete Dipole Approximation, Yurkin and Hoekstra, 2011).

The CR-SIM forward simulator is tailored to compute radar and lidar observables by integrating scattering properties over
the discrete particle size distributions (PSDs) by a constant bin size for each hydrometeor (Table 1), based on the microphysical

100 scheme used in the CRM/LES. The environmental variables are obtained/calculated from a mandatory set of model output variables consisting of pressure, temperature, dry air density, and height above sea level. The single-scattering properties are calculated using the T-matrix method and packaged as look-up tables (LUTs) in CR-SIM. The simulated idealized radar and lidar variables are provided at each model grid box and can be easily compared with real observations.

105 2.1. Scattering Properties

The LUTs compile the complex scattering amplitudes of the 2×2 scattering matrix for single non-spherical particles with equally spaced particle sizes computed using the T-matrix code of Mishchenko and Travis (1998) and Mishchenko (2000). The LUTs for each hydrometeor class corresponding to the CRM/LES simulation data (e.g., rain drop, snowflakes, cloud droplet, ice crystal, graupel) are constructed as a function of particle phase, bulk density, and aspect ratio. The bulk density used is as parameterized in the selected microphysics scheme, assuming spheroid particle shapes. For each hydrometeor class, the complex scattering amplitudes are calculated for the 91 elevation angles from 0° to 90° with a spacing of 1° , five radar frequencies at 3 GHz (S band), 5.5 GHz (C band), 9.5 GHz (X band), 35 GHz (Ka band), and 94 GHz (W band), different temperature ranges for the liquid hydrometeors, different particle densities for solid hydrometeors, and few different values of particle aspect ratio. For lidar scattering properties, the single particle extinction σ_α and backscattering cross section σ_β for spherical cloud droplets and cloud ice are calculated using the BHMIE Mie code (Bohren and Huffman, 1998). CR-SIM operates for observables from the ceilometer (wavelength of 905 nm) and micro pulse lidar (MPL, wavelengths of 353 and 532 nm).

120 Although most of the parameters related to hydrometeor particles (e.g., particle bulk density, size) required in the scattering calculations can be either computed or obtained from the prognostic and diagnostic variables from the CRMs or LESs, aspect ratios and canting angles must be assumed in the simulator and as such are prescribed by the users. All liquid and ice hydrometeors are modeled as oblate spheroids, except cloud droplets. Raindrops are represented as oblate spheroids with a size-dependent aspect ratio, following an empirical equation as a function of particle diameter based either on Brandes et al. (2002) or Andsager et al. (1999). A fixed aspect ratio is used for each solid hydrometeor category, but for graupel and hail the empirical expression proposed by Ryzhkov et al. (2011) is also available. Radar polarimetric variables depend on particle orientation, which is not information provided directly by the CRMs/LESs. For all model hydrometeors, the radar variables are calculated using complex scattering amplitudes from the pre-built LUTs, assuming a mean particle canting angle of 0° (Ryzhkov 2001) with a choice of the particle orientation distribution. The possible choices for the distribution of particle orientation model are fully (three-dimensional) random orientation, random orientation in the horizontal plane, and two-dimensional axisymmetric Gaussian distribution of orientations. In this paper, for all simulations, we used aspect ratios proposed by Brandes et al. (2002) for rain drops, 0.2 for cloud ice, 0.6 for snow, Ryzhkov et al. (2011) for graupel and hail, and the two-dimensional axisymmetric Gaussian distribution for all hydrometeor species.

135 A hydrometeor particle in CR-SIM is either pure liquid or a mixture of ice and air. The composition of particles within a
volume is accounted for in the scattering computations by an appropriate selection of the dielectric constant for different
hydrometeor types. The dielectric constant of liquid particles is frequency- and temperature-dependent (Ray, 1972). Ice phase
140 hydrometeors are assumed to be composed of ice inclusions in an ice matrix and their effective dielectric constant is computed
using the Maxwell-Garnet mixing formula (Maxwell Garnet, 1904). The output radar reflectivity (Z_{hh}) for all hydrometeor
species is the equivalent radar reflectivity, in which computations, we adopt 0.92 as the value of dielectric factor for liquid
water at centimeter wavelengths. This choice of the dielectric factor ensures a convention that the definition of radar reflectivity
reduces to form: $Z = \int N(D)D^6 dD$ for (spherical) liquid particles, where D is the droplet diameter and $N(D)$ is the droplet
145 size distribution function.

The LUTs of scattering properties incorporated in the current CR-SIM were created using the T-matrix method where
solid phase hydrometeors are represented as dielectrically dry oblate spheroids. Although these assumptions are rather simple
compared to some other radar simulators, which take into account complex electromagnetic scattering by mixed-phase
hydrometeors or ice hydrometeors with possibly irregular shapes are taken into account (e.g., Snyder et al., 2017a,b; Jiang et
145 al., 2019), such complex electromagnetic scatters can be easily incorporated by adding LUTs of their scattering properties
from different scattering calculation methods (e.g., Kneifel et al., 2017; Leinonen and Moisseev, 2015; Leinonen and Szyrmer,
2015; Lu et al., 2016) without any change to the code.

2.2. Calculations of radar and lidar observables

150 The PSD for each hydrometeor species is reproduced on the basis of the model microphysics scheme. The incorporated
microphysics schemes and corresponding CRMs currently available in CR-SIM are listed in Table 2. CRMs coupled with bulk
moment microphysics (i.e., single and double moment) basically prognose mixing ratio and, for the double moment, the
number concentration of each hydrometeor species. These parameters, in combination with assumptions used in the size
155 distribution assumptions of the microphysics scheme, determine the PSD. Bin microphysics schemes explicitly calculate the
evolution of the PSDs. Radar moment observables are computed by integrating scattering properties from the LUTs over the
discrete PSD for each hydrometeor type following Ryzhkov et al. (2011) accounting for an orientation distribution as described
in section 2.1, and then integrated over all simulated hydrometeor species to produce a unique value for each observable at
each grid box. Particle fall velocity, which is used for Doppler velocity and spectrum width computations, is parameterized as
160 a function of particle diameter in the same manner as in the selected microphysics scheme. Computed radar variables are listed
in Table 3. Figure 1 shows an example of S-band (3 GHz) radar observables from CR-SIM for a mesoscale convective system
(MCS) observed on May 20, 2011, during the Midlatitude Continental Convective Clouds Experiment (MC3E; Jensen et al.,
2016). The convective system was simulated using the Weather Research Forecasting (WRF) model (Skamarock et al., 2008)
with the Morrison 2-moment microphysics scheme, a horizontal resolution of 0.5 km, and the vertical resolution of
165 approximately 0.25 km.

CR-SIM includes a computation of the Doppler power spectra by introducing the method used in Kollias et al. (2014). Figure 2 shows examples of the Doppler spectra and its moments for the S band. In the figure, a pulse repetition frequency (PRF) of 600 Hz is used, the noise power at 1 km is -40 dB, and the number of Doppler velocity bins is 256.

170 CR-SIM also includes forward simulators for the ceilometer (wavelength of 905 nm) and ground-based micro pulse lidar (wavelengths of 532 and 353 nm). The lidar observables are computed for cloud ice and cloud droplet species (see Table 4). Figure 3 shows an example of profiles calculated for lidar observables for a cumulus case from the LES ARM Symbiotic Simulation and Observation project (LASSO, Gustafson et al., 2017) using WRF coupled with the Morrison 2-moment microphysics scheme. In this simulation, typical profiles are presented for aerosol backscatter (β_{aero}) and extinction coefficient (α_{ext_aero}), and molecular backscatter (β_{mol}) based on Spinhirne (1993). As expected, the lidar backscatter is significantly
175 attenuated by cloud droplets, but the very high lidar backscatter at the interface between air a cloud can be used to detect cloud base height.

2.3 Instrument model

180 The instrument model accounts for the effects of technological specifications on the observables, such as sampling volume and detector sensitivity. The standard output of CR-SIM consists of synthetic profiling radar and lidar observations at each grid box of the model scene, and synthetic scanning radar observations for a radar positioned at user's desired location inside the model domain. The output synthetic fields are artifact free, with no propagation or instrument sampling effects. This approach is based on the notion that the real observations used for comparison against the synthetic simulated observables will
185 have undergone rigorous post-processing that mitigate to the extent possible propagation effects, velocity folding etc. However, the user can emulate the true behavior of a scanning radar and also select where to place the radar or a network of radars within the model domain and, thus, impose preferred volume coverage pattern (VCP) scan strategy. In this case, the idealized, standard CR-SIM output at the model grid resolution can be further used as input into a radar instrument model that is written specifically for the post-processing of the CR-SIM radar simulations. The radar instrument model accounts for radar distance
190 to the target, elevation as provided by the VCP, pulse length, range resolution, antenna beamwidth, and receiver noise and output the radar observables in radar polar coordinates. For the calculation of elevation angles, the earth surface is assumed to be flat. This assumption is acceptable for general radar observation ranges (<~90 km for the vertical model grid spacing of >0.5 km). Gaussian functions are used as the antenna weighting and the range-weighting functions to estimate the contribution of the model grid observables to the radar polar coordinate system observables. Depending on the azimuthal resolution and the
195 antenna beamwidth, this instrument model also accounts for the radar sampling resolution.

The radar instrument model in its current version does not treat propagation effects. Attenuated radar reflectivity can be computed using the integrated attenuation along a radar beam path. The total (two-way) hydrometeor attenuation (A_{tot}) at each grid box is then equal to twice the sum of the specific attenuation for all simulated hydrometeors (A_h) along a radar beam path from the location of the radar to a distance of the target at r in km:

200

$$A_{tot}(r) = 2 \int_0^r A_h(r) dr \quad (1)$$

where A_{tot} is in dB and A_h in dB km⁻¹. Here gaseous attenuation was not included. The observed reflectivity Z_{hh}^{obs} (logarithmic scale) is computed by subtracting A_{tot} from Z_{hh} on a logarithmic scale:

205

$$Z_{hh}^{obs}(r) = Z_{hh}(r) - A_{tot}(r) \quad (2)$$

As well as Z_{hh} , the attenuated differential reflectivity Z_{DR}^{obs} on a logarithmic scale is calculated as:

$$Z_{DR}^{obs}(r) = Z_{DR}(r) - 2 \int_0^r A_{dp}(r) dr \quad (3)$$

where A_{dp} represents specific differential attenuation in dB km⁻¹. The minimum detectable reflectivity Z_{MIN} (logarithmic) is applied with a constant C :

$$Z_{MIN} = C + 20 \log_{10}(r) \quad (4)$$

where r is the radial distance in km, and the constant C represents the minimum detectable signal at $r = 1$ km for the pulse length selected by the user.

Figure 4 shows simulated range-height indicator (RHI) measurements at C and X bands (5.5 and 9 GHz, respectively) accounting for Z_{MIN} , hydrometeor attenuation, and the radar range-gate sampling volume for convective cells associated with an MCS observed on May 20, 2011 during MC3E. The input convective system simulation data are the same as Figure 1. The instrument specifications used for the RHI simulations are for the X-band radar, a beamwidth of 1°, range-gate spacing of 50 m, and a constant C of -50 dBZ for the Z_{MIN} calculation. The C-band radar specifications are a beamwidth of 1°, range-gate spacing of 120 m, and a constant C of -35 dBZ for the Z_{MIN} calculation. These specifications follow the X-band scanning ARM precipitation radar (X-SAPR) and C-band scanning ARM precipitation radar (C-SAPR) configurations at the ARM Southern Great Plains (SGP) site during MC3E. The results are reasonable, showing strong attenuation in Z_{hh} and Z_{DR} by rain at X band and relatively less at C band. The simulated K_{DP} at X band is approximately 1.6 times larger than that at C band because of the wavelength dependency.

230 2.4. Features of the Code

CR-SIM is written in Fortran 95 standard including all GNU extensions and parallelized with OpenMP. The input to CR-SIM is the output from the CRM/LES in NetCDF format. The output of CR-SIM is in NetCDF format and includes simulated observables for each hydrometeor specie, and one total for all the hydrometeors. These features allow users to understand contributions of each hydrometeor specie to the radar observables and a sophisticated evaluation of microphysics schemes. 235 The code includes various microphysics schemes as shown in Table 3. The code structure supports different CRMs/LESs, flexible microphysics package extensions, and diverse assumptions such as particle shape, density, and PSD for different hydrometeor categories in the models as well as different methods used for the computation of the scattering properties. The code has been released under GNU General Public License and both the software and a detailed user guide are publicly available online (Tatarevic et al., 2018).

240

3. Sample Applications of CR-SIM

In this section, several applications of CR-SIM are presented that highlight its capabilities. These applications are: i) a comparison of observed and modeled cloud fraction profiles (CFPs); ii) a quantification of uncertainty in the estimate of 245 domain-averaged CFP; iii) an evaluation of a novel retrieval technique for the estimation of cloud fraction; iv) an investigation of the impacts of limitations imposed by the nature of observations themselves on multi-Doppler wind retrieval techniques; and v) an optimization of a new radar observation strategy for multi-Doppler wind retrievals.

Figure 5 shows a flow diagram of our application processes. First, the forward simulator produces idealized observables at each model grid box (the ‘Output 1’ box in Figure 5). In the second step, an instrument model is used to account for the 250 instrument characteristics (as described in section 2.3). Third, the output from the instrument model (‘Output 2’) is then used to retrieve the CFP (the retrieval model and ‘Output 3’) for a direct comparison and, most importantly, for a quantification of the uncertainties in the cloud fraction estimates, and as well for an evaluation of the new retrieval technique (applications i – iii). On another hand, the output from the instrument model is also used as an input for multi-Doppler wind retrieval model to investigate the uncertainty of the retrieval method itself and to optimize the new radar observation strategy (applications iv 255 and v, with ‘Output 3’). The final step consists of a comparison of the retrieved quantities using a multi-Doppler wind retrieval against the input CRM/LES data, and a quantitative estimation of uncertainties attributed to the observation limitations and the retrieval algorithms. In the following subsections, we briefly describe and summarize the findings of the studies using CR-SIM.

260 3.1 Comparison of observed and modeled cloud fraction profiles

Measurements of the CFP are important to quantify the impact of shallow cumulus clouds on the grid-scale meteorological state because the fractional cloudiness of a grid box is related to effects in the radiative transfer (e.g., Albrecht 1981; Larson

et al., 2001) and the vertical cumulus mass flux (e.g., de Roode and Bretheton, 2003; van Stratum et al., 2014). Zenith-profiling
265 cloud radar and lidar measurements traditionally have been used to provide CFP estimates (e.g., Hogan et al., 2001; Kollias et
al., 2009; Remillard et al., 2013; Angevine et al., 2018). Typically, the profiling radar and lidar observations are combined
synergistically to provide a hydrometeor mask such as those described in ARSCL (Clothiaux et al., 2000) and the CloudNet
target classification (Illingworth et al., 2007). This approach takes advantage of the radar and lidar capabilities and maximizes
our ability to detect thin cloud layers. However, the performance of the combined radar/lidar algorithm degrades at heights
270 where the lidar observations are unavailable due to complete signal attenuation. These attenuation effects are naturally not
represented in model output and thus may lead to large disagreements between observations and models.

We focus here on using CR-SIM to generate a synthetic ARSCL product that is directly comparable to the ARSCL
generated using measurements from the Ka-band ARM Zenith-pointing Radar (KAZR), ceilometer, and MPL. This analysis
uses a shallow cumulus cloud field over SGP simulated by the LASSO project. The simulation is for June 27, 2015 and uses
275 WRF run as an LES coupled with the Morrison double moment microphysics scheme (Morrison et al. 2005). The horizontal
and vertical resolutions are 100 m and 20 m, respectively, and the horizontal dimension of the simulation domain is 14.4 km.

First, the KAZR, ceilometer, and MPL measurements from the ARM SGP Central Facility are simulated using the CR-
SIM forward simulator. The simulation output corresponds to the box ‘Output 2’ in Figure 5. Simulated KAZR reflectivity
accounts for attenuation (Z_{hh}^{obs}) and radar sensitivity (Z_{MIN}) as described by Eqs. (1, 2, and 4). The attenuated MPL hydrometeor
280 backscatter (β_{hydro_atten}) is obtained by subtracting β_{aero_atten} and β_{mol_atten} from β_{total_atten} , since the MPL total backscatter includes
aerosol backscatter and molecular backscatter (see Table 4). The value obtained for β_{hydro_atten} is considered to be below noise
level if less than the unattenuated background scatter ($\beta_{aero} + \beta_{mol}$), which is used in this simulation as the minimum detectable
MPL backscatter value. The ceilometer-detected first cloud base is estimated at each grid column following O’Connor et al.
(2004). Using the simulated observables, we estimate cloud locations as provided by ARSCL (‘Output 3’ in Fig. 5). A grid
285 box where either KAZR Z_{hh}^{obs} or MPL β_{hydro_atten} has a detectable value is indexed as a ‘cloudy’ grid box, and grid boxes below
the simulated ceilometer first-cloud base are indexed as ‘clear’.

An example of ARSCL simulation is shown in Fig. 6 that uses the LASSO LES data as an input. The WRF simulation
shows cumulus clouds below 5 km and cirrus clouds covering the entire domain at 12-14 km. In Figs. 6b-d, the limitation of
each instrument is represented in the forward simulations. The simulated KAZR measurements can detect cumulus cloud layers
290 but cannot detect cirrus clouds, due to their low reflectivity (lower than Z_{MIN}). Instead, the cirrus clouds can be detected by the
simulated MPL measurements. However, the cirrus clouds can be missed by both radar and lidar measurements when cumulus
clouds are present, because the MPL signal becomes fully attenuated by the low-level clouds. Figures 6f and 6g show the
domain-averaged CFPs from the LES hydrometeor mixing ratio and from the simulated ARSCL which assumes the ARM
instruments are located at every grid column (as shown in Fig. 6e). Comparison between the two CFP plots suggests that the
295 ARSCL for this LASSO case underestimates cirrus CFPs by 20%, likely due to lidar beam attenuation by lower-level cumulus
clouds that have a horizontal fraction of 20%.

3.2 Uncertainty quantification of domain-averaged cloud fraction profile estimates

300 The ARSCL product is usually integrated for 1-3 hours to provide an average CFP estimate for that time period. These CFP estimates are often compared with the model domain-averaged CFPs. However, the spatially heterogeneous distribution of the shallow cumulus clouds (Wood and Field, 2011) raises questions regarding the ability of short-term (1–3 hours) zenith-profiling observations to provide adequate sampling of the cloud field. Uncertainties in the profiling measurement of cloud fractions are introduced by the limited sampling of a highly heterogeneous cloud field. We investigate these uncertainties as a
305 function of the number of profiling sites and integration time using the CR-SIM virtual observations, using the WRF LES simulation presented in the previous application. The WRF LES output is saved every 10 minutes, and CR-SIM is run for each output file. In this analysis, we assume that no cloud evolution occurs within a 10-minute interval.

Figures 7a and 7b show the domain-averaged CFP from the simulated ARSCL and directly from the WRF using a cloud water content threshold of 0.01 g kg^{-1} . The colors indicate different integration time periods. Note that the WRF dataset in this
310 analysis is for a SGP shallow convective cloud case on June 11, 2016, different from the one used in Fig. 6, which results in higher cumulus cloud top. The simulated ARSCL CFP is in good agreement with the WRF CFP for each integrated period (compare Figs. 7a and b), indicating that uncertainties attributed to observation limitations (e.g., sensitivity and attenuation) are small. Thus, the limited spatial and/or temporal sampling is the major error source to consider when comparing the profiling measurement derived CFP with the domain-averaged WRF CFP.

315 To emulate vertical profiling measurements, we sampled data as follows. First, observation sites are randomly selected within the horizontal domain. Second, for each snapshot of the simulation, clouds over the observation sites are sampled as if the clouds are frozen in time and advected by the mean environmental wind. Thus, the columns are sampled along the direction of the horizontal wind over the advected distance (i.e. horizontal wind speed \times 10 min), where the environmental horizontal wind at each snapshot is the mean horizontal wind across the simulation domain within the cumulus cloud layer (i.e., the layer
320 between the mean cumulus cloud base and the maximum cumulus cloud top). Third and last, the CFP is estimated by varying both the number of observation sites and the integration period.

Figures 7c-h show the comparisons of the WRF CFPs and the simulated ARSCL CFPs for different number of observation sites (top row, c-e) and integration periods (bottom row, f-h). The center of integration period is 21:00 UTC. Blue lines in each panel represent the simulated ARSCL CFPs integrated over time from each selected observation site for the period indicated,
325 the red line represents the mean ARSCL CFP averaged over the sites, and the black line represents the domain-averaged WRF CFP integrated over the indicated period. Each panel shows that CFPs at a single site (blue lines) have large uncertainties even though they are integrated over long periods, ranging from 30 to 180 min. Those uncertainties are reduced when averaging the CFP profiles across the different sites; consequently, the mean CFP (red line) becomes closer to the domain-averaged WRF CFP (black lines). However, it also becomes evident that a small number of observation sites (Fig. 7c) may not be adequate to
330 estimate the true CFP.

Figures 7i and 7j show the root mean square error (RMSE) and mean absolute percentage error (MAPE) of the simulated ARSCL CFPs as a function of the number of observation sites and the integration time. Both plots show that the uncertainty can be reduced by increasing the number of observation sites and the integration period. The RMSE dramatically decreases to 0.005-0.01 (30-50 % in MAPE) when we use four observation sites and 120 min integration. The rate of improvement of CFP by further increasing the number of sites and integration period is smaller; the error values slowly decrease until the RMSE and MAPE plateau at 0.002 and 15%, respectively. However, establishing more than ten observational sites in such small domain is probably impractical. At the SGP site, five Doppler Lidar profiling measurements have already been operating over a 90 km x 90 km domain. These measurements can be effectively used to estimate cloud fraction without much uncertainty when clouds are homogeneously distributed over the domain.

3.3 Evaluation of a new CFP estimation technique using scanning cloud radar

Forward radar simulators can be used to evaluate a retrieval technique. We introduce an application to estimating CFP using scanning cloud radar (SCR) measurements based on Oue et al. (2016). As analyzed in the previous section, profiling radar measurements may include large uncertainties in CFP estimates. On the other hand, SCRs conduct observations over a domain that is much larger than can be sampled by zenith-profiling cloud radars such as KAZR (e.g., Lamer et al., 2013; Ewald et al., 2015). Although the SCRs are widely and routinely used to observe 3D cloud fields, the application of SCRs to study shallow cumuli is not straightforward. One of the most significant limitations of the SCR observations is related to the radar sensitivity. Since shallow cumuli over land typically have low reflectivities, the strong drop in SCR sensitivity with range creates the illusion of the atmosphere being cloudier closer to the radar location (e.g., Lamer and Kollias, 2015). This limitation can introduce uncertainties in the cloud fraction estimates. Oue et al. (2016) addressed uncertainties of radar-estimated CFPs due to the nature of the profiling and scanning radar techniques using CR-SIM-generated observations.

Figure 8a shows horizontal cross sections of WRF-simulated water content for a shallow convection case (June 9, 2015; Oue et al., 2016) from LASSO. Figure 8b shows the CR-SIM simulation of the Ka-band (35 GHz) Z_{hh} accounting for the minimum detectable reflectivity Z_{MIN} of the cross-wind RHI (CWRHI, Kollias et al., 2014) scans from Eq. (4) using $C=-50$ dBZ. In the CR-SIM analysis, the radar was located along the vertical line in Figure 8b, and CWRHI scans were performed along the east-west direction while the clouds were assumed to move along the north-south direction. These figures suggest that the Z_{hh} from the CWRHI scans cannot capture the clouds with lower water contents that are located far from the radar. This can affect cloud fraction estimates. Since the “true” cloud fraction is estimated from the original model cloud field and thus is known, the CR-SIM runs in different configurations can be used to establish the best method to estimate cloud fraction while accounting for limitations inherent to the nature of radar measurements. Oue et al. (2016) used the cumulative distribution function (CDF) of the observed Z_{hh} to define the size of the horizontal domain at each height needed to obtain the best estimate of the domain-averaged CFP. The horizontal domain size as a function of height corresponded to a distance from the radar where Z_{MIN} was equal to a CDF value of 10%. Figure 8c shows CFPs using a CDF of 10% when changing the

365 integration time of the CWRHI, and Figure 8d shows the RMSE of the estimated CFPs as a function of integration time, adapted from Oue et al. (2016). The figure suggests that the 35 min or longer of CWRHI measurements provide the realistic domain-averaged CFP.

3.4 Investigation of impacts of observation limitations on multi-Doppler radar wind retrievals

370

Estimation of vertical air motion is essential to understand the dynamics and microphysics of deep convective clouds (e.g., Jorgensen and LeMone, 1989), evaluate CRM and LES results (e.g., Varble et al., 2014; Fan et al., 2017), and to improve convective parameterization in global climate models (e.g., Donner et al., 2001). Multi-Doppler radar techniques have been applied to understand the dynamics and microphysics of the deep convective clouds in different climate regimes (e.g., Friedrich and Hagen, 2004; Collis et al., 2013; Oue et al., 2014). However, the multi-Doppler radar retrievals are not straightforward with potential uncertainties from multiple aspects (e.g., Clark et al., 1980; Bousquet et al., 2008; Potvin et al., 2012). CR-SIM can be used to investigate the impacts of different error sources on the retrieved wind fields.

375

Oue et al. (2019a) investigated the impacts of the radar VCP for plan position indicator (PPI) and the observation period on uncertainties in multi-Doppler radar wind retrievals using CR-SIM. They also investigated how the uncertainties attributed to the VCP period can be reduced using the advection-correction technique proposed by Shapiro et al. (2010). The advection correction scheme allows for trajectories of multiple individual clouds, performs smooth gridbox-by-gridbox corrections of cloud locations, and takes into account changes in cloud shape with time by using PPI scans at two times. We summarize their findings, particularly regarding the impacts of radar VCP and period on multi-Doppler radar retrievals.

380

Figure 9 shows a diagram of the analysis process. The input model data is a WRF simulation using the Morrison double-moment microphysics scheme for a mesoscale convective system observed on May 20, 2011, during the MC3E field campaign at the ARM SGP site. The horizontal resolution is 500 m, the vertical resolution varies from approximately 30 m near the surface to 260 m at 2 km—above which the resolution remains approximately constant, and the simulation output is saved every 20 seconds. Measurements from the three X-band scanning ARM precipitation radars (X-SAPR) at the SGP site are simulated using CR-SIM. The CR-SIM-simulated radar reflectivity and Doppler velocity at the model grid are converted into the radar polar coordinates with two different VCPs for each radar: 1) 21 elevation angles ranging from 0.5° to 45° (VCP1, same as the X-SAPR scan strategy during MC3E), and 2) 60 elevation angles ranging from 0.5° to 59.5° with a 1° increment (VCP2). For the both VCPs, the beamwidth is 1°, the range-gate spacing is 50 m, and the maximum range is 40 km. The simulated radar reflectivity and Doppler velocity in polar coordinates were used as an input to the 3DVAR multi-Doppler radar wind retrieval algorithm developed by North et al. (2017) to estimate the 3D wind field for a domain of 50 km × 50 km × 10 km with horizontal and vertical grid spacings of 0.25 km.

390

395

The convective mass flux (MF) is estimated at each height as:

$$MF = UF \bar{w} \bar{\rho}_a \quad [kg \ s^{-1} \ m^{-2}] \quad (5)$$

400 where UF is updraft fraction over the horizontal slice of the domain, \bar{w} is mean vertical velocity over the updraft area, and $\bar{\rho}_a$ is dry air density averaged over the domain. Figure 10 shows comparisons of convective mass flux profiles between simulated multi-Doppler radar retrievals and WRF output for two minimum updraft thresholds of 5 (MF_5) and 10 (MF_{10}) $m \ s^{-1}$. First, we applied the wind retrieval technique to a snapshot of the forward model output to bypass the instrument model and examine the uncertainty in the retrieval model (3FullGrid). Figure 10a shows MF profiles from the 3FullGrid simulation (red line) and 405 from WRF the snapshot (black line), 2-min average (dark gray line), and 5-min average (light gray line). The 3FullGrid MF profile is in good agreement with the WRF output which indicates that the uncertainty in the retrieval model is small; although it does underestimate the maximum MF for the updraft threshold of 5 $m \ s^{-1}$ by 0.05 $kg \ m^{-2} \ s^{-1}$ (10% of the true MF) at 5.3 km.

Figures 10b and 10c show MF profiles (MF_5 and MF_{10}) obtained from simulated retrievals while considering the effects of VCP (VCP1 and VCP2) and averaging period (snap [instantaneous], 2-min and 5-min averages). For both VCP1 (Fig. 10b) and VCP2 (Fig. 10c), the snapshot and 2-min VCP simulations have similar MF estimates for both sets of MF_5 and MF_{10} 410 curves, indicating that a 2-min average is sufficient to capture features available from an instantaneous scan. However, the accuracy of these estimates varies with MF profile and VCP. The MF_{10} estimates for both VCPs systematically underestimate the maximum values occurring between 4.5-6.5 km by about 0.5 $kg \ m^{-2} \ s^{-1}$ (20%). The performance of the MF_5 estimates for VCP snap and 2-min have strong variations with height. For VCP1 (the less dense scan pattern), MF_5 follows the WRF 415 snapshot below 4.5 km with close agreement between 3-4.5 km; however, MF is underestimated around its maximum MF by about 0.075 $kg \ m^{-2} \ s^{-1}$ (15%) and is overestimated below 3 km and above 7 km. The denser scan pattern for VCP2 provides a dramatic improvement around the maximum and above 6 km but still shows overestimations below 3 km and above 7 km. Uncertainties are often increased for the VCP simulations when the averaging period is extended to 5-min. For the 5-min VCPs, MF_{10} estimates for both VCP1 and VCP2 around the maximum are further underestimated while the MF_5 estimate for 420 VCP2 is further overestimated above 6 km. Other estimates below this height for VCP2 and for all heights for VCP1 are mostly unchanged. These results suggest that the VCP elevation strategy and sampling time extended to 5 min have a significant impact on the updraft properties retrieved at higher altitudes. This is due to density of data sampled by the VCPs, where greater density particularly improves MF_5 around its maximum, and the deformation of cloud structures within longer sampling periods (exceeding 2 min) that causes uncertainties in the mass continuity assumption.

425 The rapid volume scan of less than 5 minutes required in the retrieval of the high-quality vertical velocities is challenging for conventional scanning radars. Most of the improvements required in the sampling strategy of the observing system (higher maximum elevation angle, higher density elevation angles, and rapid VCP time period) can be accomplished using rapid scan radar systems such as the Doppler on Wheels mobile radars (DOWs, Wurman, 2001) or even phased array radar systems (e.g. Kollias et al, 2018).

430

3.5 Evaluation of new radar observation strategies

CR-SIM can also be used to examine performances of new remote sensing sensors and thus help to choose the most appropriate observation strategy for a new field campaign. Figures 4c and 4d show the performance of C-band (5.5 GHz) RHI measurements when the radar is located at 24 and 59 km away from the target convective clouds. As expected, the RHI from the greater distance provides the radar observables at lower resolution and includes more attenuation when precipitation clouds are located between the target and the radar. Oue et al. (2019a) investigated the impact of radar data sampling on the multi-Doppler radar wind retrievals for the MCS by an OSSE using CR-SIM. The addition of data from a Doppler radar to the triple-Doppler radar retrievals, shown in section 3.4, cannot significantly improve the updraft retrievals if the added radar VCP has inferior spatial resolution. Oue et al. (2019a) also showed that the updraft retrievals in a limited area around the center of the domain, where data density from the three radars are higher than other areas, produced better results than those in the entire domain. The insights obtained from these OSSEs are beneficial for decision-making regarding radar observation strategies for a field campaign, such as the number of radars required and their locations. For example, Kollias et al. (2018) used CR-SIM to examine how phased array radars improve multi-Doppler radar wind retrievals compared to scanning radars for mesoscale convective cases.

4. Summary

We presented a recently developed comprehensive forward radar and lidar simulator, CR-SIM, which is suitable for simulating complex, ground-based observational configurations and their synthetic products. CR-SIM can simulate multi-wavelength, zenith-pointing and scanning radar observables—including radar reflectivity, Doppler velocity, polarimetric fields, radar Doppler spectrum—lidar observables, and multi-sensor integrated products. The primary idea behind this simulator was to directly compare CRM/LES output with remote sensing observations such that simulated measurements are consistent with the microphysics scheme used in the model. CR-SIM incorporates microphysics and scattering properties independently so that uncertainties related to microphysical assumptions are separated from uncertainties related to scattering model. This configuration allows CR-SIM to be easily expanded, either by adding additional microphysical schemes or by adding new scattering classes.

One of the features of using CR-SIM is it produces both radar and lidar observables for all the cloud resolving model grid boxes accounting for elevation angles relative to a radar location, similar to Snyder et al. (2017a,b), rather than other radar simulators that account for radar geometry characteristics such as beamwidth and radar range resolution to simulate scatters within the radar resolution volume (e.g., Capsoni et al, 2001; Caumont et al., 2006; Cheong et al., 2008). The radar sampling characteristics are accounted for in the post-processing instrument model. This feature facilitates the process of configuring any desirable observational setup with a varying number of profiling or scanning sensors. Another feature of CR-SIM is that it can be coupled to sophisticated virtual products such as ARSCL and 3DVAR multi-Doppler based wind retrievals. The CR-

465 SIM applications shown in this paper emphasize the value of applying it to high resolution model output to emulate the
sampling of ground-based observatories. CR-SIM's coupling of CRM microphysical parameterizations with scattering models
facilitates improved evaluations of model performance by enabling robust comparisons between model-simulated clouds and
observables from radar and lidar while accounting for instrument characteristics and observation limitations. The analyses
presented here serve as a reference to the CR-SIM package and illustrate numerous applications related to sampling
470 uncertainty, sampling optimization, retrieval uncertainty, and comparison between models and observations.

List of acronyms

	ARM	Atmospheric Radiation Measurement Facility
	ARSCL	Active Remotely-Sensed Cloud Location
	CDF	Cumulative distribution function
475	CFP	Cloud fraction profile
	CRM	Cloud resolving model
	CR-SIM	Cloud resolving model Radar SIMulator
	C-SAPR	C-band scanning ARM precipitation radar
	CWRHI	Cross-wind range-height indicator
480	GCM	Global climate model
	GNU GPL	GNU General Public License
	KAZR	Ka-band ARM Zenith-pointing Radar
	LASSO	LES ARM Symbiotic Simulation and Observation
	LES	Large eddy simulation
485	LUT	Look-up table
	MAPE	Mean absolute percentage error
	MC3E	Midlatitude Continental Convective Clouds Experiment
	MCS	Mesoscale convective system
	MF	Mass flux
490	MPL	Micro pulse lidar
	OSSE	Observing system simulation experiment
	PPI	Plan position indicator
	PSD	Particle size distribution
	RHI	Range-height indicator
495	RMSE	Root mean square error
	SCR	Scanning cloud radar
	SGP	Southern Great Plains

	UF	Updraft fraction
	VCP	Volume coverage pattern
500	WRF	Weather Research Forecasting model
	X-SAPR	X-band scanning ARM precipitation radar

Code and data availability.

505 The source code for CR-SIM, along with downloading, installation instructions, and user guide is available at the Stony Brook University Academic Commons (<https://commons.library.stonybrook.edu/somasdata/4>), <https://www.bnl.gov/CMAS/cr-sim.php> (last access: September 6, 2019), and <https://you.stonybrook.edu/radar/research/radar-simulators/> (last access: September 5, 2019). The software is licensed under GNU General Public License. A code that converts model grid coordinates to radar polar coordinates is also available at the Stony Brook University Academic Commons

510 <https://commons.library.stonybrook.edu/somasdata/4> and <https://you.stonybrook.edu/radar/research/radar-simulators/> (last access: August 30, 2019). There is ongoing work to integrate this module into the CR-SIM package. The CR-SIM package available online includes a configuration file and a script to run the code. The LASSO data used in the manuscript are available at the ARM archive: <https://adc.arm.gov/lassobrowser> (ARM, 2017). All configuration files used in the simulations and other input data available online <https://commons.library.stonybrook.edu/somasdata/3> (Oue et al. 2019b).

515

Author contributions.

M. Oue and P. Kollias designed the OSSE experiments, and M. Oue carried them out. A. Tatarevic developed the radar simulator code, and with M. Oue, D. Wang, and K. Yu contributed to evolve, improve, and optimize the code. M. Oue prepared the manuscript with contributions from all co-authors.

520

Competing interests.

The authors declare that they have no conflict of interest.

525 Acknowledgements.

We would like to thank H. Morrison, Z. Feng, J. Fan, T. Matsui, and S. Endo for providing the WRF output data and for their valuable suggestions. We extend our gratitude to M. Mech and A. Hansen, P. Marinescu, and T. Yamaguchi for providing the ICON, RAMS, and SAM output data, respectively, and for their helpful comments. We would also like to thank M. I. Mishchenko for making his T-matrix codes public and freely available for research purposes and J. Vivekanandan for his

530 Mueller-matrix-based code, which was used to validate the computation of radar variables in CR-SIM. This research was

supported by the Climate Model Development and Validation activity funded by the Office of Biological and Environmental Research in the US Department of Energy Office of Science through award KP170304 (P. Kollias and A. M. Vogelmann).

References

- 535 Albrecht, B. A.: Parameterization of trade-cumulus cloud amounts. *J. Atmos. Sci.*, 38, 97-105, doi: 10.1175/1520-0469(1981)038<0097:POTCCA>2.0.CO;2, 1981.
- Angevine, W, Olson, J., Kenyon, J., Gustafson, W., Endo, S., Suselj, K., and Turner, D.: Shallow cumulus in WRF parameterizations evaluated against LASSO large-eddy simulations, *Mon. Wea. Rev.*, doi:10.1175/MWR-D-18-0115.1, 2018.
- 540 Andsager, K., Beard, K. V., and Laird N. F.: Laboratory measurements of axis ratios for large drops, *J. Atmos. Sci.*, 56, 2673–2683, doi: 10.1175/1520-0469(1999)056<2673:LMOARF>2.0.CO;2, 1999.
- Atmospheric Radiation Measurement (ARM) Research Facility. September 2017. LASSO Data Bundles., 36° 36' 18.0" N, 97° 29' 6.0" W: Southern Great Plains Central Facility (C1). Compiled by WI Gustafson, AM Vogelmann, X Cheng, S Endo, KL Johnson, B Krishna, Z Li, T Toto, and H Xiao. ARM Data Archive: Oak Ridge, Tennessee, USA. Data set accessed at <http://dx.doi.org/10.5439/1342961>.
- 545 Bohren, C. F. and Huffman, D. R.: Absorption and scattering of light by small particles, New York : Wiley, 1998, 530 p., ISBN 0-471-29340-7, ISBN 978-0-471-29340-8 (second edition).
- Bousquet, O., Tabary, P., and Parent du Châtelet, J.: Operational multiple-Doppler wind retrieval inferred from long-range radial velocity measurements, *J. Appl. Meteor. Climatol.*, 47, 2929-2945, doi: 10.1175/2008JAMC1878.1, 2008.
- 550 Brandes, E. A., Zhang, G., and Vivekanandan, J.: Experiments in rainfall estimation with a polarimetric radar in a subtropical environment, *J. Appl. Meteor.*, 41, 674–685, doi: 10.1175/1520-0450(2002)041<0674:EIREWA>2.0.CO;2 2002.
- Capsoni, C., D'Amico, M., and Nebuloni, R.: A Multiparameter Polarimetric Radar Simulator. *J. Atmos. Oceanic Technol.*, 18, 1799–1809, [https://doi.org/10.1175/1520-0426\(2001\)018<1799:AMPRS>2.0.CO;2](https://doi.org/10.1175/1520-0426(2001)018<1799:AMPRS>2.0.CO;2), 2001.
- Caumont, O., Ducrocq, V., Delrieu, G., Gosset, M., Pinty, J., Parent du Châtelet, J., Andrieu, H., Lemaître, Y., and Scialom, G.: A Radar Simulator for High-Resolution Nonhydrostatic Models. *J. Atmos. Oceanic Technol.*, 23, 1049–1067, <https://doi.org/10.1175/JTECH1905.1>, 2006.
- 555 Cheong, B.L., Palmer, R.D., and Xue, M.: A Time Series Weather Radar Simulator Based on High-Resolution Atmospheric Models. *J. Atmos. Oceanic Technol.*, 25, 230–243, <https://doi.org/10.1175/2007JTECHA923.1>, 2008.
- Clark, T. L., Harris, F. I., and Mohr, C. G.: Errors in wind fields derived from multiple-Doppler radars: Random errors and temporal errors associated with advection and evolution, *J. Appl. Meteor.*, 19, 1273–1284, 1980.
- 560 Clothiaux, E. E., Ackerman, T. P., Mace, G. G., Moran, K. P., Marchand, R. T., Miller, M. A., and Martner, B. E.: Objective determination of cloud heights and radar reflectivities using a combination of active remote sensors at the ARM CART sites, *J. Appl. Meteor.*, 39(5), 645-665, doi: 10.1175/1520-0450(2000)039<0645:ODOCHA>2.0.CO;2, 2000.
- Clothiaux, E. E., Miller, M. A., Perez, R. C., Turner, D. D., Moran, K. P., Martner, B. E., Ackerman, T. P., Mace, G. G., Marchand, R. T., Widener, K. B., Rodriguez, D. J., Uttal, T., Mather, J. H., Flynn, C. J., Gaustad, K. L., and Ermold, B.: The ARM Millimeter Wave Cloud Radars (MMCRs) and the Active Remote Sensing of Clouds (ARSCL) Value Added Product (VAP), DOE Tech. Memo. ARM VAP-002.1, 2001.
- 565 Collis, C., Protat, A., May, P. T., and Williams, C.: Statistics of storm updraft velocities from TWP-ICE including verification with profiling measurements, *J. Appl. Meteor. Climatol.*, 52, 1909-1922, doi: 10.1175/JAMC-D-12-0230.1, 2013.
- Cotton, W. R. et al.: RAMS 2001: Current status and future directions, *Meteorol. Atmos. Phys.*, 82(1), 5–29, doi:10.1007/s00703-001-0584-9, 2003.

- de Roode, S. R., and Bretherton C. S.: Mass-flux budgets of shallow cumulus clouds. *J. Atmos. Sci.*, **60**, 137–151, doi: 10.1175/1520-0469(2003)060<0137:MFBOSC>2.0.CO;2, 2003.
- 575 Donner, L. J., Seman, C. J., Hemler, R. S., and Fan, S.: A cumulus parameterization including mass fluxes, convective vertical velocities, and mesoscale effects: Thermodynamic and hydrological aspects in a general circulation model, *J. Climate*, **14**, 3444–3463, doi: 10.1175/1520-0442(2001)014<3444:ACPIMF>2.0.CO;2, 2001.
- Doviak, R. J., and Zrníc, D. S.: Doppler radar and weather observations, 2nd ed., San Diego, Academic Press, Second Addition, 2006.
- Ewald, F., Winkler, C., and Zinner, T.: Reconstruction of cloud geometry using a scanning cloud radar, *Atmos. Meas. Tech.*, **8**, 2491–2508, doi:10.5194/amt-8-2491-2015, 2015.
- 580 Fan, J., Han, B., Varble, A., Morrison, H., North, K., Kollias, P., Chen, B., Dong, X., Giangrande, S. E., Khain, A., Lin, Y., Mansell, E., Milbrandt, J. A., Stenz, R., Thompson, G., and Wang, Y.: Cloud-resolving model intercomparison of an MC3E squall line case: Part I—Convective updrafts, *J. Geophys. Res. Atmos.*, **122**, 9351–9378, doi:10.1002/2017JD026622, 2017.
- 585 Fan, J., Leung, L. R., Li, Z., Morrison, H., Chen, H., Zhou, Y., Qian, Y., and Wang, Y.: Aerosol impacts on clouds and precipitation in eastern China: Results from bin and bulk microphysics, *J. Geophys. Res.*, **117**, D00K36, <https://doi.org/10.1029/2011JD016537>, 2012.
- Feingold, G., Kreidenweis, S. M., Stevens, B., and Cotton, W. R.: Numerical simulations of stratocumulus processing of cloud condensation nuclei through collision-coalescence, *J. Geophys. Res.*, **101**(D16), 21,391–21,402, doi:10.1029/96JD01552, 1996.
- 590 Friedrich, K. and Hagen, M.: Wind synthesis and quality control of multiple-Doppler-derived horizontal wind fields, *J. Appl. Meteor.*, **43**, 38–57, doi:10.1175/1520-0450(2004)043<0038:WSAQCO>2.0.CO;2, 2004.
- Gustafson, W.I., Vogelmann, A.M., Cheng, X., Dumas, K.K., Endo, S., Johnson, K.L., Krishna, B., Li, Z., Toto, T., and Xiao, H.: Description of the LASSO Data Bundles Product. DOE Atmospheric Radiation Measurement user facility, DOE/SC-ARM-TR-216, <http://dx.doi.org/10.2172/1469590>, 2019.
- 595 Gustafson Jr., W. I., Vogelmann, A. M., Cheng, X., Endo, S., Krishna, B., Li, Z., Toto, T., Xiao, H.: Recommendations for Implementation of the LASSO Workflow, DOE/SC-ARM-17-031, doi:10.2172/1406259, 2017.
- Hogan, R. J., Jakob, C., and Illingworth, A. J.: Comparison of ECMWF Winter-Season Cloud Fraction with Radar-Derived Values. *J. Appl. Meteorol.*, **40**, 513–525, doi:[http://dx.doi.org/10.1175/1520-0450\(2001\)040<0513:COEWSC>2.0.CO;2](http://dx.doi.org/10.1175/1520-0450(2001)040<0513:COEWSC>2.0.CO;2), 2001
- 600 Illingworth, A., Hogan, R., O'connor, E., Bouniol, D., Brooks, M., Delanoë, J., Donovan, D., Eastment, J., Gaussiat, N., Goddard, J. W., and co-authors, CLOUDNET Continuous evaluation of cloud profiles in seven operational models using ground-based observations, *Bull. Amer. Meteor. Soc.*, **88**(6), 883–898, doi: <https://doi.org/10.1175/BAMS-88-6-883>, 2007.
- Jensen, M. P., Petersen, W. A., Bansemer, A., Bharadwaj, N., Carey, L. D., Cecil, D. J., Collis, S. M., Del Genio, A. D., Dolan, B., Gerlach, J., Giangrande, S. E., Heymsfield, A., Heymsfield, G., Kollias, P., Lang, T. J., Nesbitt, S. W., Neumann, A., Poellot, M., Rutledge, S. A., Schwaller, M., Tokay, A., Williams, C. R., Wolff, D. B., Xie, S., and Zipser, E. J.: The Midlatitude Continental Convective Clouds Experiment (MC3E), *Bull. Amer. Meteor. Soc.*, **1667**–1686, doi: 10.1175/BAMS-D-14-00228.1, 2016.
- Jiang, Z., Kumjian, M.R., Schrom, R.S., Giammanco, I., Brown-Giammanco, T., Estes, H., Maiden, R., and Heymsfield, A.J.: Comparisons of Electromagnetic Scattering Properties of Real Hailstones and Spheroids. *J. Appl. Meteor. Climatol.*, **58**, 93–112, <https://doi.org/10.1175/JAMC-D-17-0344.1>, 2019.
- 610 Jorgensen, D. P. and LeMone, M. A.: Vertically velocity characteristics of oceanic convection, *J. Atmos. Sci.*, **46**, 621–640, doi: 10.1175/1520-0469(1989)046<0621:VVCOOC>2.0.CO;2, 1989.
- Kneifel, S., Dias Neto, J., Ori, D., Moisseev, D., Tyynelä, J., Adams, I. S., Kuo, K.-S., Bennartz, R., Berne, A., Clothiaux, E. E., Eriksson, P., Geer, A. J., Homeyager, R., Leinonen, J., and Westbrook, C. D.: The first international summer snowfall

- 615 workshop: Scattering properties of realistic frozen hydrometeors from simulations and observations, as well as defining a new standard for scattering databases. *Bulletin of the American Meteorological Society*. doi:10.1175/BAMS-D-17-0208.1, 2018
- Kneifel, S., Lerber, A., Tiira, J., Moisseev, D., Kollias, P., and Leinonen, J.: Observed relations between snowfall microphysics and triple-frequency radar measurements. *Journal of Geophysical Research*, 120, 6034–6055, doi:10.1002/2015JD023156, 620 2015.
- Kneifel, S., Kollias, P., Battaglia, A., Leinonen, J., Maahn, M., Kalesse, H., and Tridon, F.: First observations of triple frequency radar Doppler spectra in snowfall: Interpretation and applications. *Geophysical Research Letters*, 43, 2225–2233, doi:10.1002/2015GL067618, 2016.
- Kollias, P., McLaughlin, D. J., Frasier, S., Oue, M., Luke, E., and Sneddon, A.: Advances and applications in low-power 625 phased array X-band weather radars. Proc. 2018 IEEE Radar Conference, Oklahoma City, OK, USA, doi: 10.1109/RADAR.2018.8378762, 2018.
- Kollias, P., Miller, M. A., Johnson, K. L., Jensen, M. P., and Troyan, D. T.: Cloud, thermodynamic, and precipitation observations in West Africa during 2006. *J. Geophys. Res. Atmos.*, 114, D00E08, doi:10.1029/2008JD010641, 2009.
- Kollias, P., and Tanelli, S., Battaglia, A., Tatarevic, A.: Evaluation of EarthCARE cloud profiling radar Doppler velocity 630 measurements in particle sedimentation regimes. *J. Atmos. Oceanic Technol.*, 31, 366–386, doi: 10.1175/JTECH-D-11-00202.1, 2014.
- Lamer, K., Fridlind, A. M., Ackerman, A. S., Kollias, P., Clothiaux, E. E., and Kelley, M.: (GO)2-SIM: a GCM-oriented ground-observation forward-simulator framework for objective evaluation of cloud and precipitation phase. *Geosci. Model Dev.*, 11, 4195–4214, <https://doi.org/10.5194/gmd-11-4195-2018>, 2018.
- 635 Lamer, K., and Kollias, P.: Observations of fair-weather cumuli over land: Dynamical factors controlling cloud size and cover, *Geophys. Res. Lett.*, 42, 8693–8701, doi: 10.1002/2015GL064534, 2015.
- Lamer, K., Tatarevic, A., Jo, I., and Kollias P.: Evaluation of gridded Scanning ARM Cloud Radar reflectivity observations and vertical Doppler velocity retrievals, *Atmos. Meas. Tech.*, 7, 1089–1103, doi:10.5194/amt-7-1089-2014, 2013.
- Larson, V. E., Wood, R., Field, P. R., Golaz, J.-C., Vonder Haar, T. H., and Cotton W. R.: Small-scale and mesoscale variability 640 of scalars in cloudy boundary layers: One-dimensional probability density functions., *J. Atmos. Sci.*, 58, 1978–1994, doi: 10.1175/1520-0469(2001)058<1978:SSAMVO>2.0.CO;2, 2001.
- Leinonen, J., and Moisseev, D.: What do triple-frequency radar signatures reveal about aggregate snowflakes? *Journal of Geophysical Research: Atmospheres*, 120, 229–239. doi:10.1002/2014JD022072, 2015.
- Leinonen, J., and Szyrmer, W: Radar signatures of snowflake riming: A modeling study. *Earth and Space Science*, 2(8), 346–645 358. doi:10.1002/2015EA000102, 2015
- Löhnert, U., Schween, J. H., Acquistapace, C., Ebell, K., Maahn, M., Barrera-Verdejo, M., Hirsikko, A., Bohn, B., Knaps, A., O’connor, E., Simmer, C., Wahner, A., and Crewell, S.: JOYCE: Jülich Observatory for Cloud Evolution, *Bull. Amer. Meteor. Soc.*, 96, 1157–1174, doi:10.1175/BAMS-D-14-00105.1, 2015.
- Lu, Y., Jiang, Z., Aydin, K., Verlinde, J., Clothiaux, E. E., and Botta, G.: A polarimetric scattering database for non- 650 spherical ice particles at microwave wavelengths. *Atmospheric Measurement Techniques*, 9(10), 5119–5134. <https://doi.org/10.5194/amt-9-5119-2016>, 2016
- Luke, E., Kollias, P., and Shupe, M.: Detection of supercooled liquid in mixed-phase clouds using radar Doppler spectra. *J. Geophys. Res. Atmos.*, 115, D19201, doi:10.1029/2009JD012884, 2010.
- Mather, J. H., Turner, D. D., and Ackerman, T. P.: Scientific maturation of the ARM Program. The Atmospheric Radiation Measurement (ARM) Program: The First 20 Years, Meteor. Monogr., No. 57, *Amer. Meteor. Soc.*, doi: 655 10.1175/AMSMONOGRAPHS-D-15-0053.1, 2016.
- Matrosov, S.Y., Schmitt, C.G., Maahn, M., and de Boer, G.: Atmospheric ice particle shape estimates from polarimetric radar measurements and in situ observations. *J. Atmos. Oceanic Technol.*, 34, 2569–2587, doi: <https://doi.org/10.1175/JTECH-D-17-0111.1>, 2017.

- 660 Matsui, T., Dolan, B., Rutledge, S. A., Tao, W.-K., Iguchi, T., Barnum, J., and Lang, S. E.: POLARRIS: A POLARimetric Radar Retrieval and Instrument Simulator. *Journal of Geophysical Research: Atmospheres*, 124, 4634–4657. Doi: <https://doi.org/10.1029/2018JD028317>, 2019
- Maxwell Garnet, J. C.: Colours in Metal Glasses and in Metallic Films. *Philosophical Transactions of the Royal Society of London. Series A, Containing Papers of a Mathematical or Physical Character*, 203, pp. 385–420. JSTOR, www.jstor.org/stable/90866, 1904
- 665 Milbrandt, J. A., and Yau, M. K.: A multimoment bulk microphysics parameterization. Part I: Analysis of the role of the spectral shape parameter. *J. Atmos. Sci.*, 62, 3051–3064, <https://doi.org/10.1175/JAS3534.1>, 2005a.
- Milbrandt, J. A., and Yau, M. K.: A multimoment bulk microphysics parameterization. Part II: A proposed three-moment closure and scheme description. *J. Atmos. Sci.*, 62, 3065–3081, <https://doi.org/10.1175/JAS3535.1>, 2005b.
- 670 Mishchenko, M. I. and Travis, L. D.: Capabilities and limitations of a current FORTRAN implementation of the T-matrix method for randomly oriented, rotationally symmetric scatterers, *J. Quant. Spectrosc. Radiat. Transfer*, 60, 309–324, [https://doi.org/10.1016/S0022-4073\(98\)00008-9](https://doi.org/10.1016/S0022-4073(98)00008-9), 1998.
- Mishchenko, M. I.: Calculation of the amplitude matrix for a nonspherical particle in a fixed orientation. *Appl. Opt.*, 39, 1026–1031, <https://doi.org/10.1364/AO.39.001026>, 2000.
- 675 Morrison, H., Curry, J. A., and Khvorostyanov, V. I.: A new double-moment microphysics parameterization for application in cloud and climate models. Part I: Description. *J. Atmos. Sci.*, 62, 1665–1677, <https://doi.org/10.1175/JAS3446.1>, 2005.
- Morrison, H. and Milbrandt, J. A.: Parameterization of cloud microphysics based on the prediction of bulk Ice particle properties. Part I: Scheme description and idealized tests. *J. Atmos. Sci.*, 72, 287–311, <https://doi.org/10.1175/JAS-D-14-0065.1>, 2015.
- 680 North, K. W., Oue, M., Kollias, P., Giangrande, S. E., Collis, S. M., and Potvin, C. K.: Vertical air motion retrievals in deep convective clouds using the ARM scanning radar network in Oklahoma during MC3E, *Atmos. Meas. Tech.* 10, 1 – 14, doi: 10.5194/amt-10-2785-2017, 2017.
- O'Connor, E. J., Illingworth, A. J., and Hogan, R. J.: A technique for autocalibration of cloud lidar, *J. Atmos. Ocean. Tech.*, 21, 777–786, doi: 10.1175/1520-0426(2004)021<0777:ATFAOC>2.0.CO;2, 2004.
- 685 Oue, M., Inagaki, K., Shinoda, T., Ohigashi, T., Kouketsu, T., Kato, M., Tsuboki, K., Uyeda H.: Polarimetric Doppler radar analysis of organization of a stationary rainband with changing orientations in July 2010, *J. Meteorol. Soc. Jpn.*, 22, 457–481, doi: 10.2151/jmsj.2014-503, 2014.
- Oue, M., Kollias, P., North, K. W., Tatarevic, A., Endo, S., Vogelmann, A. M., and Gustafson Jr., W. I.: Estimation of cloud fraction profile in shallow convection using a scanning cloud radar. *Geophys. Res. Lett.*, 43, 10998–11006, doi: 10.1002/2016GL070776, 2016.
- 690 Oue, M., Kollias, P., Shapiro, A., Tatarevic, A., and Matsui, T.: Investigation of observational error sources in multi-Doppler-radar three-dimensional variational vertical air motion retrievals, *Atmos. Meas. Tech.*, 12, 1999–2018, <https://doi.org/10.5194/amt-12-1999-2019>, 2019a.
- Oue, M., Matsui, T., and Kollias, P.: Configuration files and input data used for radar simulations described in "The Cloud Resolving Model Radar Simulator (CR-SIM) Version 3.2: Description and Applications of a Virtual Observatory" SoMAS Research Data. 3. <https://commons.library.stonybrook.edu/somasdata/3>, 2019b.
- 695 Potvin, C. K., Wicker, L. J., and Shapiro A.: Assessing errors in variational dual-Doppler wind syntheses of supercell thunderstorms observed by storm-scale mobile radars, *J. Atmos. Ocean. Tech.*, 29, 1009–1025, doi: 10.1175/JTECH-D-11-00177.1, 2012.
- 700 Ray, P. S.: Broadband complex refractive indices of ice and water. *Applied optics*, 11(8), 1836–1844, 1972.
- Rémillard, J., Kollias, P., and Szyrmer, W.: Radar-radiometer retrievals of cloud number concentration and dispersion parameter in non drizzling marine stratocumulus, *Atmos. Meas. Tech.*, 6, 1817–1828, doi:10.5194/amt-6-1817-2013, 2013

- Ryzhkov, A. V.: Interpretation of polarimetric radar covariance matrix for meteorological scatterers: Theoretical analysis. *J. Atmos. Oceanic Technol.*, 18, 315–328, [https://doi.org/10.1175/1520-0426\(2001\)018<0315:IOPRCM>2.0.CO;2](https://doi.org/10.1175/1520-0426(2001)018<0315:IOPRCM>2.0.CO;2), 2001.
- 705 Ryzhkov A. V., Pinsky, M., Pokrovsky, A., and Khain, A.: Polarimetric Radar Observation Operator for a Cloud Model with Spectral Microphysics. *J. Appl. Meteor. Climatol.*, 50, 873–894, <https://doi.org/10.1175/2010JAMC2363.1>, 2011.
- Seifert, A.: On the parameterization of evaporation of raindrops as simulated by a one-dimensional rainshaft model, *J. Atmos. Sci.*, 65, 3608–3619, <https://doi.org/10.1175/2008JAS2586.1>, 2008.
- Seifert, A. and Beheng, K. D.: A two-moment cloud microphysics parameterization for mixed-phase clouds. Part I: Model description. *Meteorol. Atmos. Phys.*, 92, 45–66, <https://doi.org/10.1007/s00703-005-0112-4>, 2006.
- 710 Shapiro, A., Willingham, K. M., and Potvin, C. K.: Spatially variable advection correction of radar data. Part I: Theoretical considerations, *J. Atmos. Sci.*, 67, 3445–3456, doi: 10.1175/2010JAS3465.1, 2010a.
- Shupe, M. D.: A ground-based multiple remote-sensor cloud phase classifier, *Geophys. Res. Lett.*, 34, L22809, doi:10.1029/2007GL031008, 2007.
- 715 Skamarock, W. C., Klemp, J. B., Dudhia, J., Gill, D. O., Barker, D. M., Duda, M. G., Wang, W., and Powers, J. G.: A description of the advanced research WRF version 3. NCAR Technical Note, NCAR/TN-475+STR, National Center for Atmospheric Research, 113 pp, <https://doi.org/10.5065/D68S4MVH>, 2008.
- Snyder, J. C., Bluestein, H. B., Dawson II, D. T., and Jung, Y.: Simulations of polarimetric, X-band radar signatures in supercells. Part I: Description of experiment and simulated ρ_{hv} rings. *J. Appl. Meteorol. Climatol.*, 56, 1977 – 1999, doi: 10.1175/JAMC-D-16-0138.1, 2017a.
- 720 Snyder, J. C., Bluestein, H. B., Dawson II, D. T., and Jung, Y.: Simulations of polarimetric, X-band radar signatures in supercells. Part II: Z_{DR} columns and rings and K_{DP} columns. *J. Appl. Meteorol. Climatol.*, 56, 1977 – 1999, doi: 10.1175/JAMC-D-16-0139.1, 2017b.
- Spinhirne, J. D.: Micro Pulse Lidar. *IEEE Transactions on Geoscience and Remote Sensing*, 31, 48–55, 1993.
- 725 Stevens, B., Farrell, D., Hirsch, L., Jansen, F., Nuijens, L., Serikov, I., Brüggmann, B., Forde, M., Linne, H., Lonitz, K., and Prospero, J. M.: The Barbados cloud Observatory: Anchoring investigations of clouds and circulation on the edge of the ITCZ, *Bull. Amer. Meteor. Soc.*, 97, 787–801, doi: 10.1175/BAMS-D-14-00247.1, 2016.
- Szyrmer, W., Tatarevic, A., and Kollias, P.: Ice clouds microphysical retrieval using 94-GHz Doppler radar observations: Basic relations within the retrieval framework, *J. Geophys. Res. Atmos.*, 117, D14203, doi:10.1029/2011JD016675_2012
- 730 Szyrmer, W. and Zawadzki, I.: *J. Atmos. Sci.*, 71, 1171–1186, Snow Studies. Part IV: Ensemble Retrieval of Snow Microphysics from Dual-Wavelength Vertically Pointing Radars, *J. Atmos. Sci.*, 71, 1171–1186, <https://journals.ametsoc.org/doi/abs/10.1175/JAS-D-12-0286.1>, 2014.
- Tatarevic, A., Kollias, P., Oue, M., Wang, D., and Yu, K.: User’s Guide CR-SIM SOFTWARE v 3.1, Brookhaven National Laboratory - Stony Brook University - McGill University Radar Science Group, 2018. [Available at <https://www.bnl.gov/CMAS/cr-sim.php>; <https://you.stonybrook.edu/radar/research/radar-simulators/>.]
- 735 Thompson, G., Field, P. R., Rasmussen, R. M., and Hall, W. D.: Explicit forecasts of winter precipitation using an improved bulk microphysics scheme. Part II: Implementation of a new snow parameterization. *Mon. Wea. Rev.*, 136, 5095–5155, 2008.
- Turner, D.D. and Ellingson, R.G.: Introduction. *Meteorological Monographs*, 57, v–x, <https://doi.org/10.1175/AMSMONOGRAPHS-D-16-0001.1>, 2016.
- 740 Tzivion, S., Feingold, G., and Levin, Z.: An efficient numerical solution to the stochastic collection equation, *J. Atmos. Sci.*, 44, 3139–3149, doi: 10.1175/1520-0469(1987)044<3139:AENSTT>2.0.CO;2, 1987.
- Yurkin, M. A., and A. G. Hoekstra, 2011: The discrete-dipole-approximation code ADDA: Capabilities and known limitations. *J. Quant. Spectrosc. Radiat. Transfer*, 112, 2234–2247, doi: 10.1016/j.jqsrt.2011.01.031.
- 745 Von Lerber, A., Moisseev, D., Bliven, L., Petersen, W., Harri, A., and Chandrasekar, V.: Microphysical properties of snow and their link to $Z_e - S$ relations during BAECC 2014. *J. Appl. Meteorol.*, 56, 1561 – 1582, 2017.

- van Stratum, B. J. H., Vilá-Guerau de Arellano, J., van Heerwaarden, C. C., and Ouwersloot, H. G.: Subcloud-layer feedbacks driven by the mass flux of shallow cumulus convection over land. *J. Atmos. Sci.*, **71**, 881–895, doi: 10.1175/JAS-D-13-0192.1, 2014.
- 750 Varble, A., Zipser, E. J., Fridlind, A. M., Zhu, P., Ackerman, A. S., Chaboureau, J.-P., Collis, S., Fan, J., Hill, A., and Shipway, B.: Evaluation of cloud-resolving and limited area model intercomparison simulations using TWP-ICE observations: 1. Deep convective updraft properties, *J. Geophys. Res. Atmos.*, 119, 13,891–13,918, doi:10.1002/2013JD021371, 2014.
- Wood, R., and Field, P. R.: The distribution of cloud horizontal sizes. *J. Clim.*, 24, 4800-4816, doi: 10.1175/2011JCLI4056.1, 2011.
- 755 Zhang, D., Wang, W., Heymsfield, A., Fan, J., and Luo, T.: Ice concentration retrieval in stratiform mixed-phase clouds using cloud radar reflectivity measurements and 1d ice growth model simulations. *J. Atmos. Sci.*, 71, 3613–3635, doi:10.1175/JAS-D-13-0354.1, 2014.
- Zhang, Y., Xie, S., Klein, S. A., Marchand, R., Kollias, P., Clothiaux, E. E., Lin, W., Johnson, K., Swales, D., Bodas-Salcedo, A., Tang, S., Haynes, J. M., Collis, S., Jensen, M., Bharadwaj, N., Hardin, J., and Isom, B.: The ARM cloud radar simulator for global climate models., *Bull. American Meteorol. Soc.*, 99, 21 – 26, doi: 10.1175/BAMS-D-16-0258.1, 2018.
- 760 Wurman, J., The DOW mobile multiple-Doppler network. Preprints, 30th Int. Conf. on Radar Meteorology, Munich, Germany, Amer. Meteor. Soc., 95–97, 2001.

Tables

765

Table 1. The minimum and maximum sizes and bin spacing of simulated particles for each hydrometeor category from the bulk microphysics schemes except the P3 scheme. ‘Particle size’ here refers to the particle maximum dimension.

Category	Minimum size [μm]	Maximum size [μm]	Bin spacing [μm]
Cloud	1	250	1
Drizzle	1	250	1
Rain	100	9000	20
Ice	1	1496	5
Snow, aggregates	100	50000	100
Graupel	5	50005	100
Hail	5	50005	100

770

Table 2. Incorporated microphysics schemes and corresponding CRMs.

CRM	Microphysics scheme (M=moment)
Weather Research and Forecasting Model (WRF)	Morrison 2-M scheme (Morrison et al. 2005)
	Milbrandt and Yau multi-M scheme (Milbrandt and Yau 2005a, 2005b)
	Thompson 1- and 2-M scheme (Thompson et al. 2008)
	Predicted particle properties (P3) scheme (Morrison and Milbrandt 2015)
	Spectral bin microphysics (Fan et al. 2012)
ICOsahedral Non-hydrostatic general circulation model (ICON)	Seifert and Beheng 2-M scheme (Seifert and Beheng 2006; Seifert 2008)
Regional Atmospheric Modeling System (RAMS)	2-M scheme (Cotton et al., 2003)
System for Atmospheric Modeling (SAM)	Tel Aviv University 2-M bin microphysics (Tzivion et al. 1987; Feingold et al. 1996)
	Morrison 2-M scheme (Morrison et al. 2005)

Table 3. Computed radar variables. Units the variables stored in output files are provided in square brackets.

Variable	Description
Z_{hh}	Radar reflectivity factor at horizontal polarization [dBZ]
Z_{vv}	Radar reflectivity factor at vertical polarization [dBZ]
Z_{vh}	Cross-polarization radar reflectivity factor [dBZ]
Z_{DR}	Differential reflectivity, defined as the ratio between the fraction of horizontally polarized backscattering and vertically polarized backscattering [dB]
LDR_h	Linear depolarization ratio, defined as the ratio of the power backscattered at vertical polarization to the power backscattered at horizontal polarization for a horizontally polarized field [dB]
K_{DP}	Specific differential phase, the backward propagation phase difference between the horizontally and vertically polarized waves at a specific distance [$^{\circ} \text{ km}^{-1}$]
δ	Differential backscatter phase, defined as the difference between the phases of horizontally and vertical polarized components of the wave caused by backscattering from the objects in the radar resolution volume, computed based on Trömel et al (2013) [$^{\circ}$]
A_h	Specific attenuation at horizontal polarization, or for horizontally polarized waves, represented by forward scattering amplitudes [dB km^{-1}]
A_v	Specific attenuation at vertical polarization, or for vertically polarized waves, represented by forward scattering amplitudes [dB km^{-1}]
A_{DP}	Specific differential attenuation, defined as the difference between the specific attenuations for horizontally and vertically polarized waves [dB km^{-1}]
V_D	Mean radial Doppler velocity (positive away from the radar) [m s^{-1}]
$V_{D_{90}}$	Mean vertical Doppler velocity (positive upward) [m s^{-1}]
SW_{TOT}	Spectrum width, including contribution of four major spectral broadening mechanisms (Doviak and Zrníc, 2006): 1) different hydrometeor terminal velocity of different sizes SW_H , 2) turbulence, 3) mean wind shear contribution, and 4) cross wind contribution. Antenna motion and contributions due to variation of orientation and vibrations of hydrometeor are not considered. [m s^{-1}]
$SW_{H_{90}}$	Spectrum width due to different hydrometeor terminal velocity of different sizes in vertical, such that $SW_{H_{90}} = SW_H (\theta=90^{\circ})$, where θ is the elevation angle measured from horizontal [m s^{-1}]
V_{RW}	Reflectivity weighted velocity (positive downward) [m s^{-1}]
Z_{MIN}	Radar minimum detectable reflectivity [dBZ]
Spectra_ Z_{hh}	Radar Doppler spectra at horizontal polarization [$\text{m s}^{-1} \text{ dB}^{-1}$]
Spectra_ Z_{vv}	Radar Doppler spectra at vertical polarization [$\text{m s}^{-1} \text{ dB}^{-1}$]
Spectra_ Z_{vh}	Cross-polarization radar Doppler spectra [$\text{m s}^{-1} \text{ dB}^{-1}$]

Table 4. Computed lidar variables

Variable	Description
$\beta_{hydro}, \beta_{aero}, \beta_{mol}$	Backscatter [$\text{sr}^{-1} \text{m}^{-1}$] for cloud droplets and cloud ice (β_{hydro}), aerosols (β_{aero}), and air molecules (β_{mol})
$\beta_{hydro_atten}, \beta_{aero_atten}, \beta_{mol_atten}$	Attenuated backscatter [$\text{sr}^{-1} \text{m}^{-1}$] for cloud droplets and cloud ice (β_{hydro_atten}), aerosols (β_{aero_atten}), and air molecules (β_{mol_atten})
$\alpha_{ext_hydro}, \alpha_{ext_aero}$	Extinction coefficient [m^{-1}] for cloud droplets and cloud ice (α_{ext_hydro}) and aerosols (α_{ext_aero})
β_{total}	Total backscatter [$\text{sr}^{-1} \text{m}^{-1}$], defined as $\beta_{total} = \beta_{hydro} + \beta_{aero} + \beta_{mol}$
β_{total_atten}	Attenuated total backscatter [$\text{sr}^{-1} \text{m}^{-1}$], defined as $\beta_{total_atten} = \beta_{hydro_atten} + \beta_{aero_atten} + \beta_{mol_atten}$
S	Lidar ratio, defined as $S = \alpha_{ext_hydro} / \beta_{hydro}$

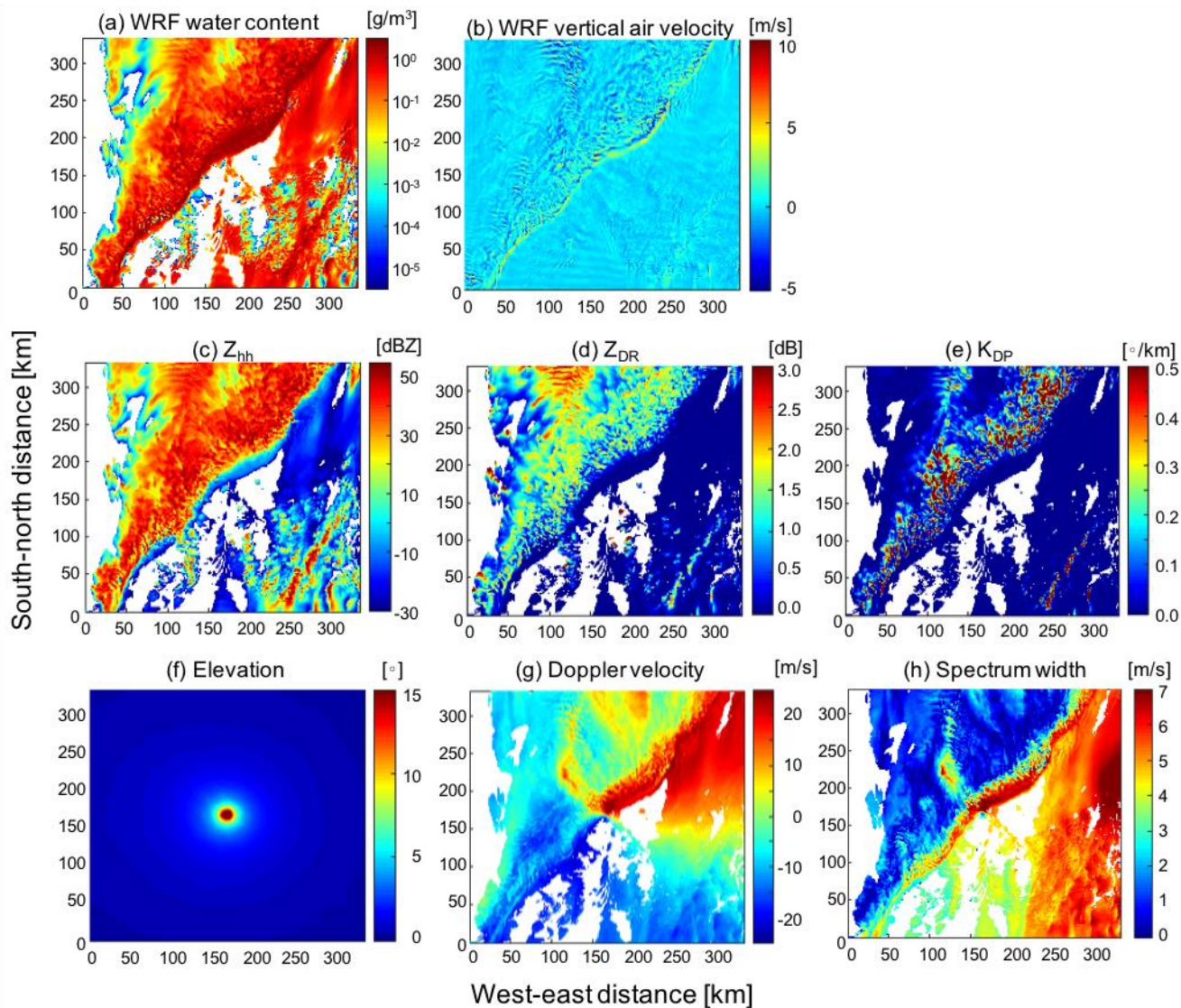
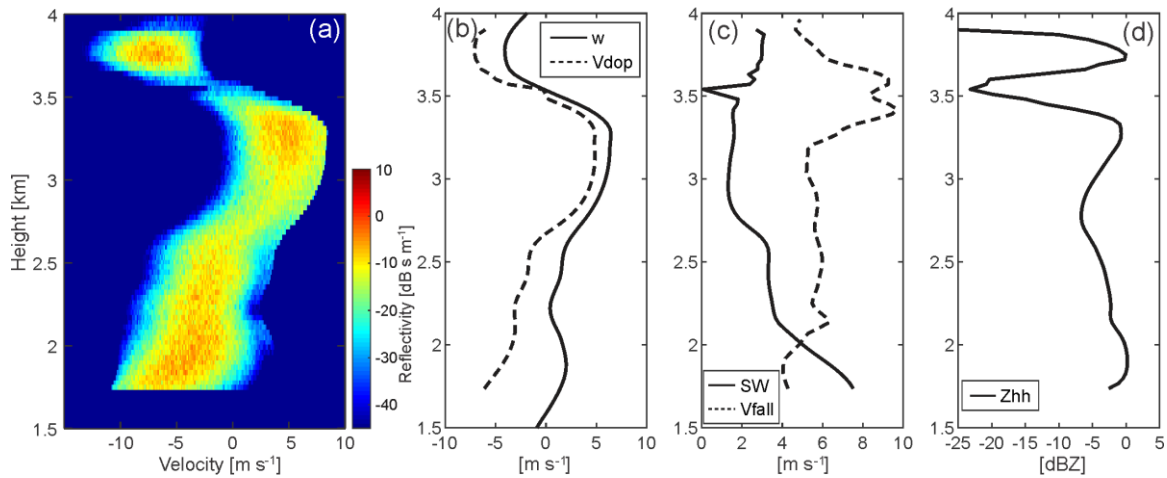
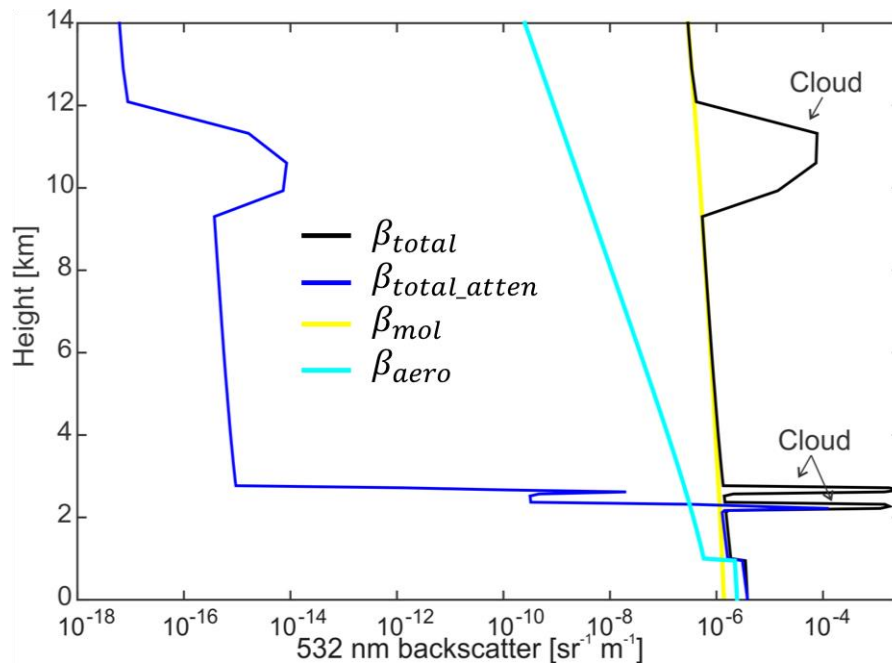


Figure 1: Radar observables produced by CR-SIM for a mesoscale convective system. The system was simulated using WRF with the Morrison 2-moment microphysics scheme at 1.8 km altitude. Shown are horizontal cross sections of (a) total hydrometeor content and (b) vertical air velocity from the WRF simulation. CR-SIM produces the following parameters for a scanning S-band (3 GHz) radar located at the center of the domain: (c) Z_{hh} , (d) Z_{DR} , (e) K_{DP} , (f) radar antenna elevation angle, (g) Doppler velocity, and (h) spectrum width at 12:18:00 UTC.

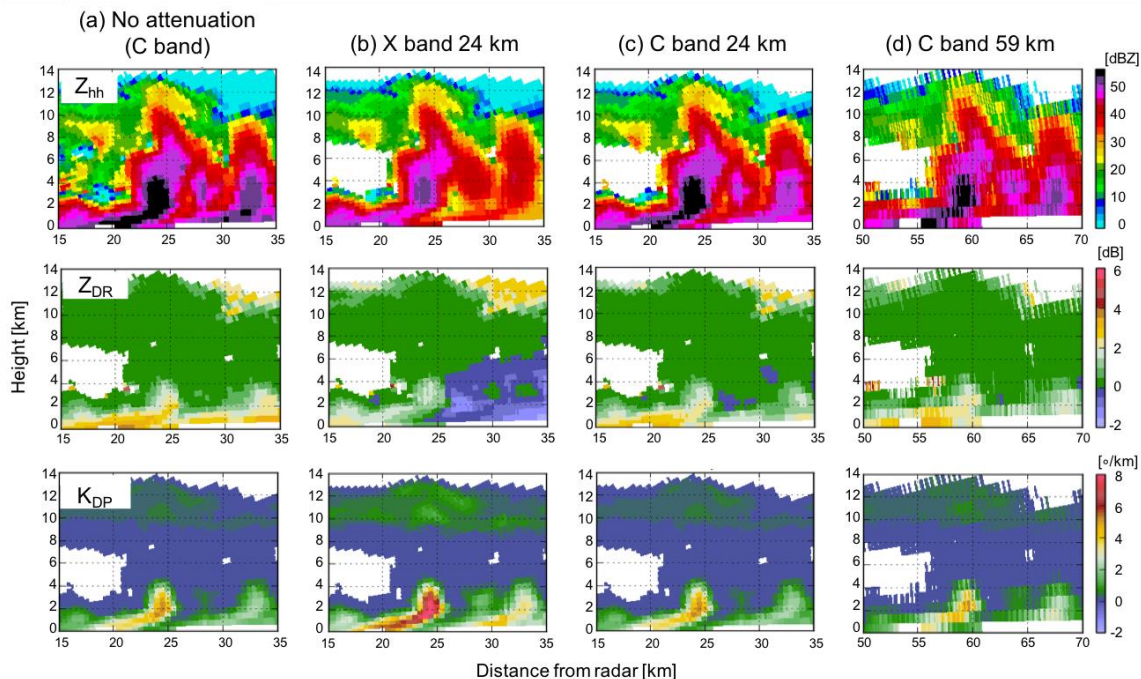


795 **Figure 2: CR-SIM examples of radar observables for a shallow convection LASSO case from a WRF simulation coupled with the Thompson microphysics scheme. Shown are (a) simulated radar Doppler spectra, (b) model vertical velocity (w , solid line) and simulated mean Doppler velocity (V_{dop} , dashed line), (c) simulated spectrum width (SW , solid line) and simulated reflectivity-weighted velocity (V_{fall} , dashed line), and (d) simulated total reflectivity (Z_{hh}) at S band (3 GHz). In (a) and (b), a positive sign indicates upward motion, and in (c), a positive sign indicates downward motion (fall speed).**

800

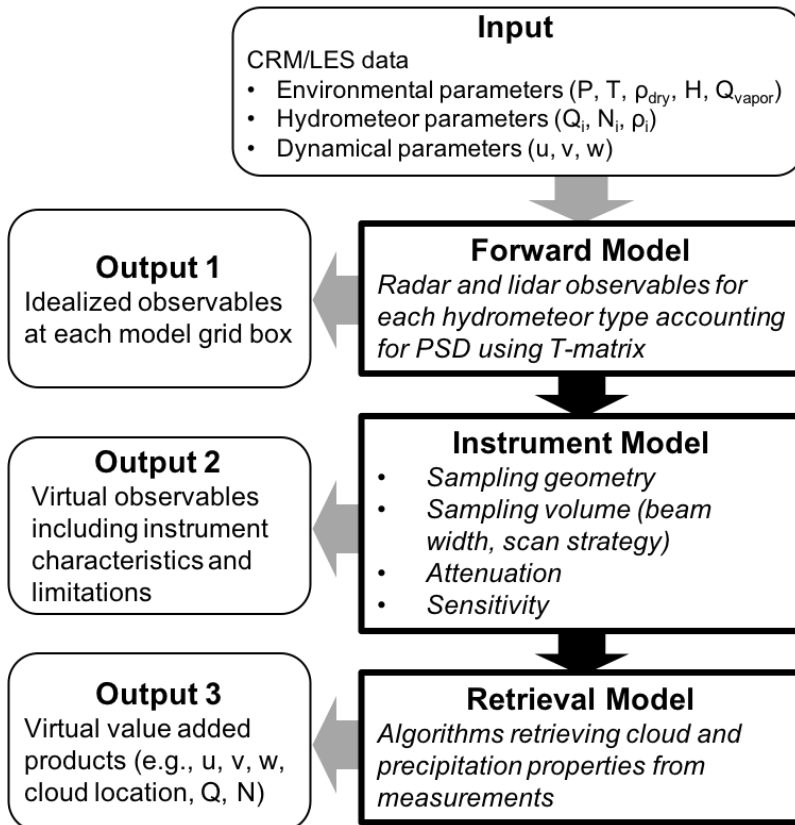


805 **Figure 3: Lidar observables from CR-SIM for a cumulus case from LASSO using WRF with the Morrison 2-moment microphysics scheme. Example of simulated vertical profiles are shown for β_{total} , β_{total_atten} , β_{mol} , and β_{aero} at a wavelength of 532 nm.**



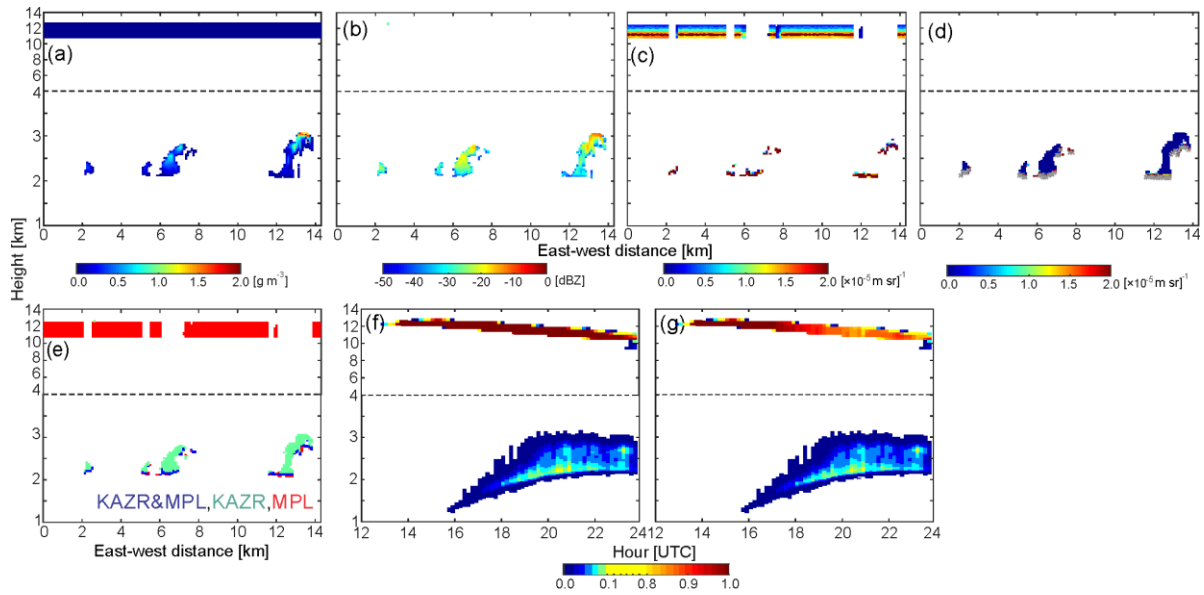
810 **Figure 4: Examples of C- and X-band (5.5 and 9 GHz, respectively) RHI scans with a beamwidth of 1° produced using CR-SIM for a convective cell in a mesoscale convective system (MCS). The simulation uses WRF with the Morrison double moment microphysics scheme for an MCS on May 20, 2011 during MC3E. Shown are variables at X- and C-band frequencies 15-35 km from the radar as a function of height at 12:18:00 UTC: (top row) Z_{hh} , (middle row) Z_{DR} , and (bottom row) K_{DP} . The figure shows (a) C-band variables without attenuation, (b) X-band variables with attenuation from a radar 24 km from the convective cell, (c) C-band variables with attenuation from a radar 24 km away, and (d) C-band variables from a radar located 59 km away with attenuation.**

815



820 **Figure 5: Diagram for CR-SIM and its applications. The diagram indicates the CR-SIM input and the different levels of output for the forward model, instrument model, and retrieval model.**

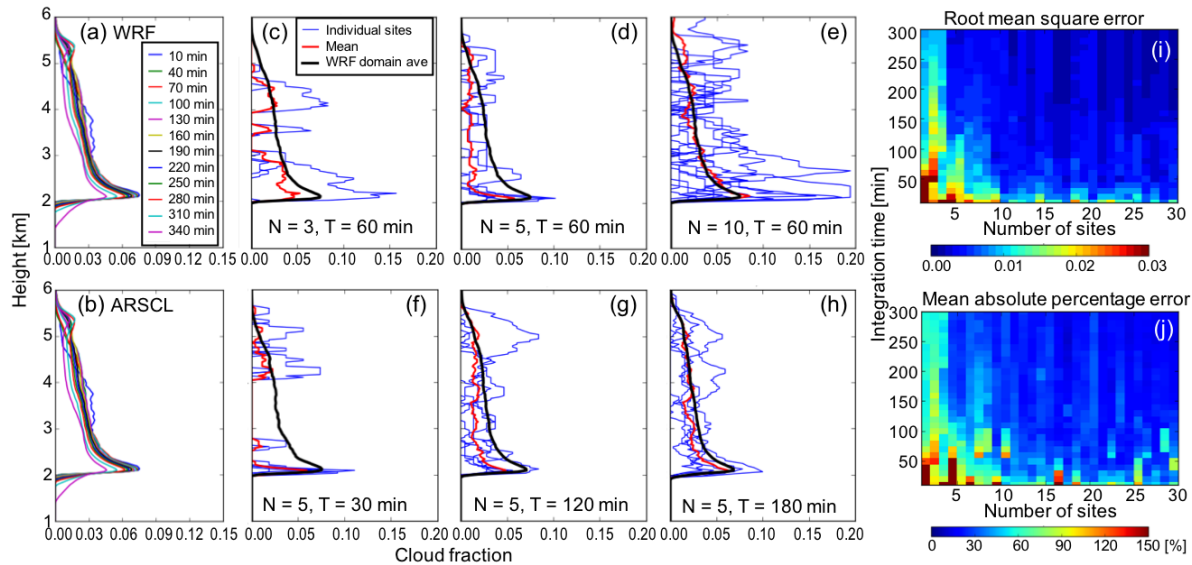
825



830

Figure 6: Simulated vertically pointing radar and lidar measurements and the ARSCL product for a shallow convection case on June 27, 2015. (a-e) Vertical cross sections of (a) water content from the WRF model, (b) Ka-band (35 GHz) radar reflectivity accounting for radar sensitivity and attenuation, (c) MPL attenuated backscatter, (d) ceilometer backscatter (colorbar) and first cloud base (gray dots), and (e) the ARSCL cloud mask. (f,g) Height-versus-time cross sections of domain-averaged cloud fraction from (f) WRF water content $> 0.001 \text{ g m}^{-3}$ and (g) the simulated ARSCL product.

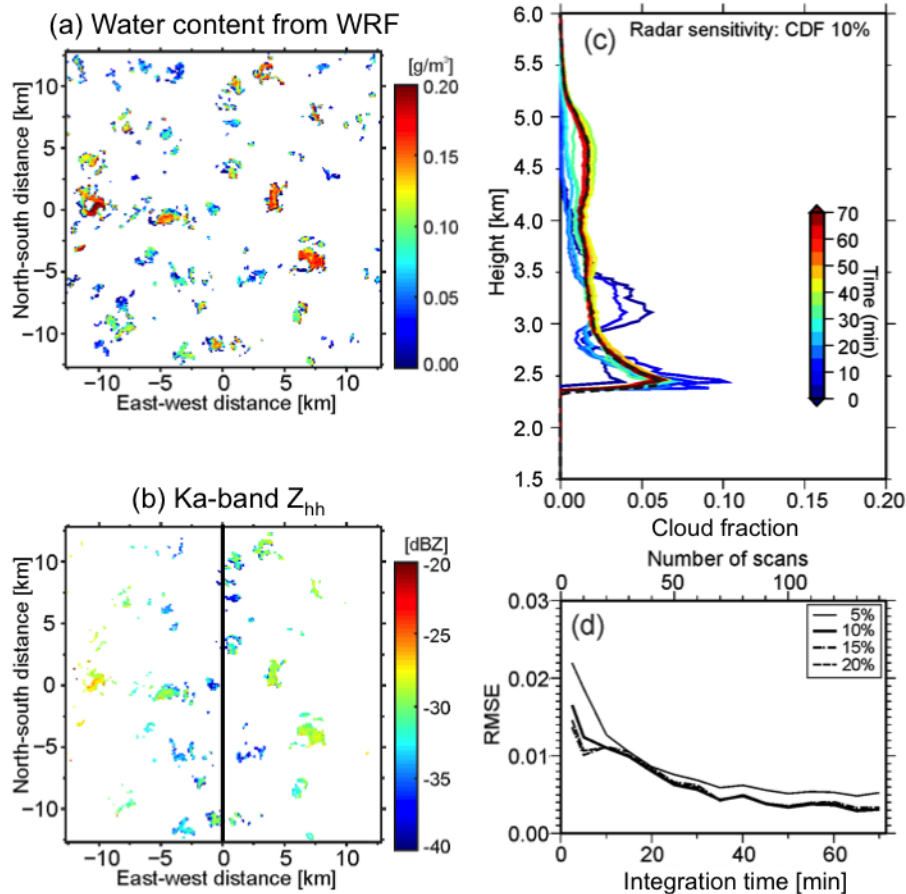
835



845

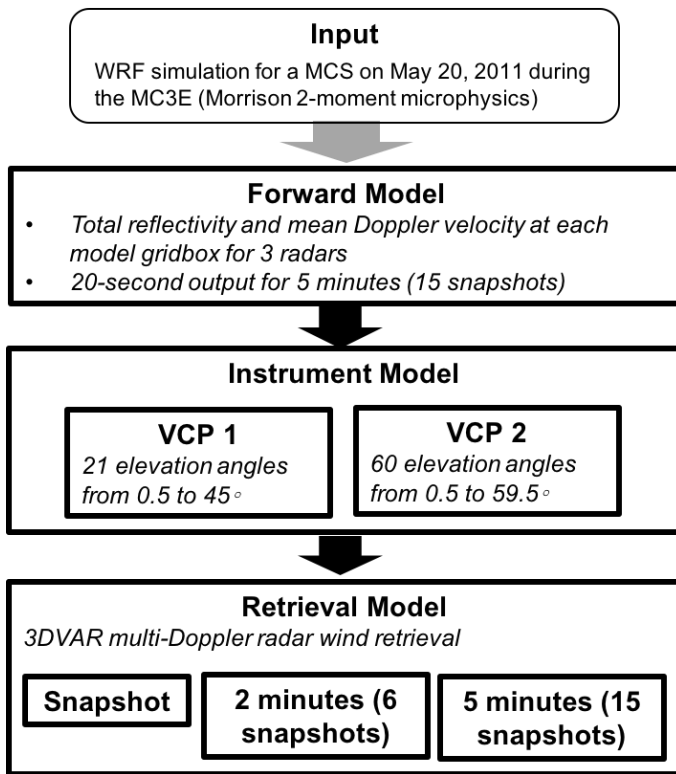
850

Figure 7: Investigation of errors of cloud fraction profiles (CFPs) from profiling measurements. CFPs from single sites are estimated by integrating over time, and then they are averaged over site. Shown are domain-averaged cloud fraction profiles (CFPs) from (a) WRF-simulated cloud water mixing ratio and (b) the simulated ARSCL product for a shallow convection case on June 11, 2016. Colors in (a) and (b) represent different integration time periods centered at 21:00:00 UTC. The minimum threshold for the WRF cloud water mixing ratio is 0.01 g kg^{-1} . (c-h) CFPs from the simulated ARSCL with different number of observation sites N and different integration periods T . The black line in (c-h) represents the domain-averaged CFP from the WRF-simulated cloud water mixing ratio, blue lines represent CFPs from individual observation sites, and the red line represents the mean CFP from averaging over the individual sites. (i and j) Root mean square error (i) and mean absolute percentage error (j) of the simulated ARSCL CFPs as a function of the number of observation sites and integration period.



855 **Figure 8: Horizontal cross sections of (a) water content simulated by WRF and (b) Ka-band (35 GHz) Z_{hh} simulated at 2.4 km above ground level for a LASSO case. In (b), it is assumed that the radar is located at $x=0$ km and the RHI is scanned along the east-west axis, and the radar sensitivity Z_{MIN} with $Z_0 = -50$ dBZ was applied. (c) Cloud fraction profiles corresponding to the 10% cumulative distribution function (CDF) isoline with changing integration time of CWRHI (hence, number of scans). (d) The root-mean-square error (RMSE) from the LES domain-averaged CFP for CDF isolines of 5% (thin solid line), 10% (thick solid line), 15% (dashed line), and 20% (dashed-dotted line) as a function of integration time. The black dashed line in (c) represents the LES domain-averaged CFP for hydrometeor mixing ratio ≥ 0.01 g kg^{-1} . (c) and (d) are adapted from Oue et al. (2016).**

860



865

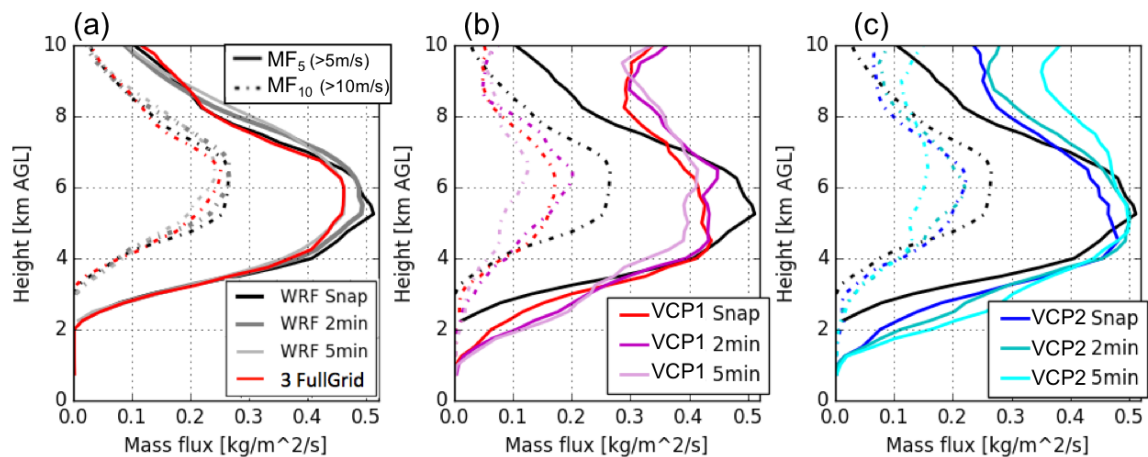
Figure 9: A diagram of an Observing System Simulation Experiment study to investigate the impacts of radar volume coverage pattern (VCP) on a multi-Doppler radar wind retrieval.

870

875

880

885



890 **Figure10: Vertical profiles of convective mass flux with different updraft thresholds of 5 m s^{-1} (solid lines) and 10 m s^{-1} (dashed lines). Displayed in each panel are different retrieval simulations represented by different colors. The dark gray line in (a) represents the time average of the WRF output over 2 minutes, and the light gray line in (a) represents the time average of the WRF output over 5 minutes. The profile from the WRF snapshot is displayed in each panel by a black solid line. Adapted from Oue et al. (2019a).**

895

900